Chemical Engineering Journal 446 (2022) 137158

Contents lists available at ScienceDirect

Chemical Engineering Journal

journal homepage: www.elsevier.com/locate/cej

Conjugated microporous polymers incorporating Thiazolo[5,4-*d*]thiazole moieties for Sunlight-Driven hydrogen production from water

Maha Mohamed Samy [a,b,1], Islam M.A. Mekhemer [b,c,1], Mohamed Gamal Mohamed [a,b,*], Mohamed Hammad Elsayed [c], Kun-Han Lin [d], Yi-Kuan Chen [e], Tien-Lin Wu [e], Ho-Hsiu Chou [c,*], Shiao-Wei Kuo [a,f,*]

[a] Department of Materials and Optoelectronic Science, Center of Crystal Research, National Sun Yat-Sen University, Kaohsiung 804, Taiwan
[b] Chemistry Department, Faculty of Science, Assiut University, Assiut 71516, Egypt
[c] Department of Chemical Engineering, National Tsing Hua University, Hsinchu 30013, Taiwan
[d] Max Planck Institute for Polymer Research, Ackermannweg 10, 55128 Mainz, Germany
[e] Chemistry Department, National Tsing Hua University, Hsinchu 30013, Taiwan
[f] Department of Medicinal and Applied Chemistry, Kaohsiung Medical University, Kaohsiung 807, Taiwan

ARTICLE INFO

Keywords:
Conjugated microporous polymers (CMPs)
Donor-acceptor system
Thiazolo[5,4-*d*]thiazole unit
Hydrogen evolution
Apparent quantum yield

ABSTRACT

In this paper, we describe efficient, inexpensive, and donor–acceptor (D–A) systems based on conjugated microporous polymers incorporating thiazolo[5,4-*d*]thiazole (ThTh) linkages for the extraction of H_2 from H_2O under visible light in the presence of ascorbic acid (AA) as a sacrificial electron donor without additional noble metals as co-catalyst. The integration of electron-rich pyrene (Py) and electron-deficient ThTh units in Py-ThTh-CMP resulted in a D–A system that provided an H_2 evolution rate (HER) of 1874 μmol $g^{-1}h^{-1}$; this value was greater than those of the other tested CMPs prepared with and without the ThTh acceptor moiety. Notably, Py-ThTh-CMP also exceeded the HERs of many other reported materials for photocatalytic H_2O reduction, including co-catalysts based on covalent organic frameworks, CMPs, and graphitic carbon nitride. The DFT and TD-DFT suggested the incorporation of ThTh moiety in the CMPs backbone to enhance the charge transfer via S1 ↔ T1 and contribute to the H_2 formation. This study presents a new approach for preparing highly efficient photocatalysts for the practical development of cost-effective H_2 evolution.

1. Introduction

Because hydrogen (H_2) is becoming a practical alternative to fossil fuels and an environmentally friendly form of energy [1–4], the generation of H_2 gas photo catalytically from the splitting of water (H_2O) is becoming more attractive in the quest for sustainable energy [5–10]. Inorganic semiconductors have mostly been used as photocatalysts to produce H_2 gas, owing to their high activity and stability [11–16]. Nevertheless, inorganic photocatalysts (e.g., metal oxides, sulfides, oxysulfides, nitrides) have some limitations in terms of the efficiency of their H_2 evolution, difficulties in their preparation, and their weak absorption of visible light, and, possibly, the low abundance of their natural resources. Recent studies have suggested that organic photocatalysts could become the best systems for the production of H_2 gas due to the availability of their building units, the ease and diversity of their preparation, the flexibility of their molecular design, and the feasible tuning of their electronic structures and band gaps [17–19]. Many organic photocatalysts have been demonstrated to produce H_2 from H_2O, including graphitic carbon nitride (g-C_3N_4), polymer dots, linear polymers, covalent organic frameworks (COF), metal–organic frameworks (MOFs), hydrophilic polymers, covalent triazine frameworks (CTFs), and conjugated microporous polymers (CMPs) [20–22]. In particular, CMPs are types of porous polymers that have garnered great attention recently because of their high surface areas and porosities, superior chemical stability, and tunable and robust properties [23,24]. Many procedures and building units have been developed to provide CMPs with applications in, for example, energy storage, luminescence, catalysis, light emission, sensing, light-harvesting, dye and

* Corresponding authors at: Department of Materials and Optoelectronic Science, Center of Crystal Research, National Sun Yat-Sen University, Kaohsiung, Taiwan (M.G. Mohamed and S.W. Kuo).
E-mail addresses: mgamal.eldin12@aun.edu.eg (M.G. Mohamed), hhchou@mx.nthu.edu.tw (H.-H. Chou), kuosw@faculty.nsysu.edu.tw (S.-W. Kuo).
[1] These authors contributed equally to this work.

https://doi.org/10.1016/j.cej.2022.137158
Received 23 February 2022; Received in revised form 18 May 2022; Accepted 21 May 2022
Available online 23 May 2022

iodine capture, encapsulation, and gas separation and capture [25–45]. CMPs have also found applications in semiconductor photocatalysis, owing to their large delocalized π-electron systems and compressible band gaps [46,47]. Many CMPs have also been designed for photocatalytic purposes, including H_2 evolution, amine oxidation, oxygen and indole activation, sulfide oxidation, and cycloaddition [48–54]. The fabrication of novel molecular building blocks capable of high photocatalytic performance has become a goal in CMP research. Likewise, CMPs containing donor (D) and acceptor (A) units have become targets for photocatalysis because of their potential for mediating charge transfer processes. The thiazolo[5,4-*d*]thiazole (ThTh) moiety has been used as a common A unit in CMPs because of its ease of preparation, high stability against oxidation, and outstanding electron-withdrawing characteristics, rigidity, and planarity. Accordingly, ThTh-linked polymers have been applied widely in optoelectronics, photovoltaics, gas separation, fluorescence, and electrical conductivity [55–58]. Recently, ThTh-based CMPs have been employed as semiconductor photocatalysts, taking advantage of their extended intermolecular π–π overlap, high light-absorbing capability, low bandgap energies, and high charge carrier mobilities. For example, Zhao et al. constructed two photoactive ThTh-CMPs using a metal-free method and then explored their photocatalytic efficiency in reducing CO_2 [59]. Tan and co-workers reported that the ThTh-containing CMP TZCP-3 exhibited high photodegradation efficiency because the ThTh moieties improved the absorption of visible light and, consequently, enhanced the photocatalytic activity [60]. Lang et al. found that TzTz-CMP-2 had outstanding activity (<90%) in the oxidation of amines into imines when using EtOH as the redox solvent; they attributed this behavior to the porosity and flexibility of the ThTh ring [61]. Furthermore, the Wen group prepared a two-dimensional COF photocatalyst containing pyrene (Py) and thiazolo[5,4-*d*]thiazole (Tz) units that displayed excellent ability for H_2 evolution through H_2O splitting [62]. Lotsch et al. described a TpDTz-COF system that provided a good rate of H_2 production (941 μmol h^{-1} g^{-1}) in H_2O when using triethanolamine as a sacrificial agent and a Ni-thiolate cluster (NiME) cluster as the co-catalyst [63]. Khan et al. reported that the CMP CNU-$TT_{12.0}$, prepared through co-polymerization to introduce ThTh units within a polymeric carbon nitride (PCN) framework, exhibited good photocatalytic characteristics for H_2O degradation [64]. However, only a few papers have described the effects of incorporating ThTh moiety within CMP skeletons to produce H_2 through H_2O splitting. Accordingly, in this study, we fabricated three photoactive ThTh-CMPs containing electron donor moieties (thiophene, biphenyl, pyrene) connected to ThTh units as electron acceptor moieties for the production of H_2 through H_2O degradation. We obtained these three ThTh-CMPs through condensation reactions of dithiooxamide with the three aromatic aldehydes Ts-Ph-CHO, Bi-Ph-CHO, and Py-Ph-CHO, respectively, in DMF (Scheme 1). We used Fourier transform infrared (FTIR) spectroscopy, ^{13}C NMR spectroscopy, Brunauer–Emmett–Teller (BET) analysis, photoluminescence (PL) spectroscopy, transmission electron microscopy (TEM), and scanning electron microscopy (SEM) to investigate the chemical structures, surface areas, morphologies, thermal stabilities, and photoelectric characteristics of these three new ThTh-CMPs. We then examined the activities of the ThTh-CMPs as photocatalysts for the generation of H_2 through the splitting of H_2O when using ascorbic acid (AA) as the sacrificial electron donor (SED). Notably, our ThTh-CMPs exhibited excellent photocatalytic performance for the reduction of H_2O to produce H_2 without the need for any additional co-catalysts.

2. Experimental

2.1. Materials

Dichloromethane (DCM), methanol (MeOH), tetrahydrofuran (THF), chloroform ($CHCl_3$), *N*, *N*-dimethylformamide (DMF), 1,4-dioxane, acetone, hydrochloric acid (HCl), 4-formylphenylboronic acid, 4-bromophenylboronic acid, potassium carbonate (K_2CO_3), $Pd(PPh_3)_4$, thiophene, 4,4́-biphenol, bromine (Br_2), iodomethane, dithiooxamide, sodium hydroxide (NaOH), and sodium bicarbonate ($NaHCO_3$) were purchased commercially (Alfa Aesar, Acros, Sigma–Aldrich). 1,3,6,8-

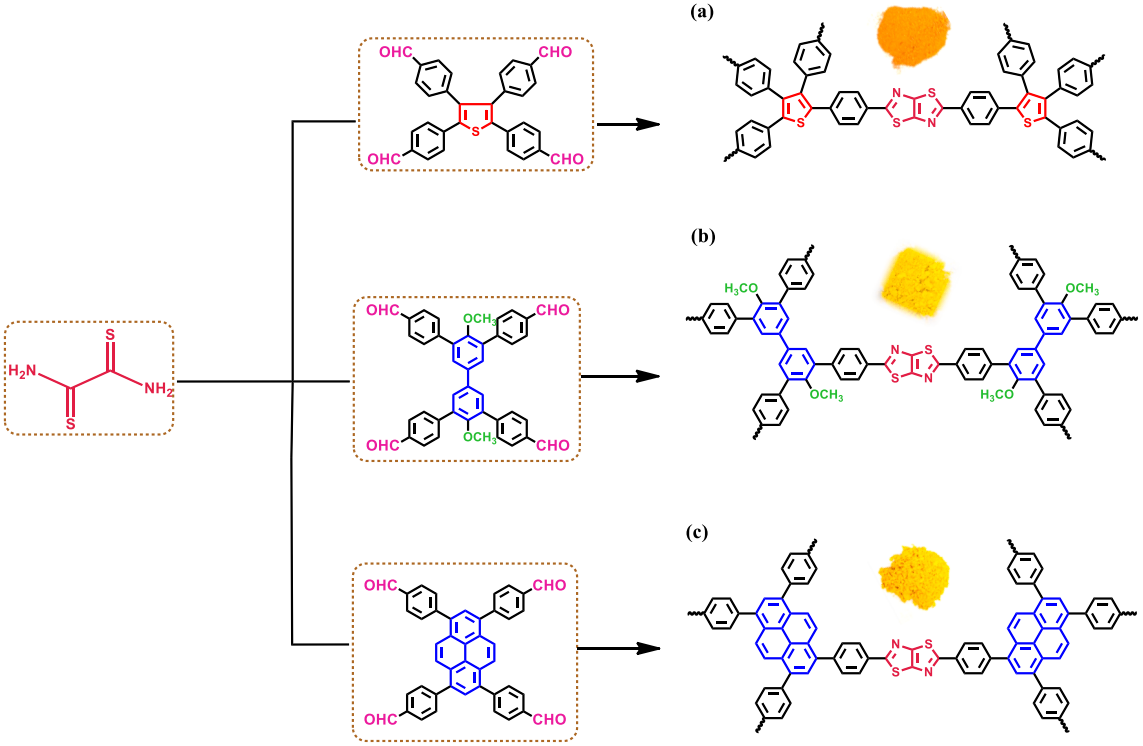

Scheme 1. Synthesis of (a) Ts-ThTh-CMP, (b) Bi-ThTh-CMP, and (c) Py-ThTh-CMP.

Tetrabromopyrene (Py-Br_4) and 1,3,6,8-tetra(4-formylphenyl)pyrene (Py-Ph-CHO) were synthesized according to previously reported procedures [65,66]. Py-PhPh-CMP was prepared according to a previously reported method [67].

2.2. Synthetic methods of monomers and CMPs

2.2.1. Synthesis of 2,3,4,5-Tetrabromothiophene (Ts-4Br)

Br_2 (5.3 mL, 0.033 mmol) was added slowly to a solution of thiophene (2.0 g, 0.023 mmol) in $CHCl_3$ (15 mL) at 0 °C, and then the mixture was heated under reflux for 6 h. NaOH solution (100 mL) was added, and the mixture was heated under reflux for 6 h. After cooling, the product was filtered off, washed with H_2O, and dried. FTIR (KBr, cm^{-1}, Figure S1): 1636 (C = C), 852 (C–S), 735 (C–Br). ^{1}H NMR (500 MHz, DMSO, δ, ppm, Figure S2): No signals observed. ^{13}C NMR (125 MHz, $CDCl_3$, δ, ppm, Figure S3): 116.936, 110.284. HR-FD-MS: *m/z*: 398.242 (Figure S4). Anal. Calcd for C_4Br_4S: C, 12.02; S, 8.02 %. Found: C, 12.13; S, 8.11%.

2.2.2. Synthesis of 2,3,4,5-Tetra(4-formylphenyl)thiophene (Ts-Ph-CHO)

A mixture of Ts-4Br (0.54 g, 1.4 mmol), $Pd(PPh_3)_4$ (0.06 g, 0.05 mmol), 4-formylphenylboronic acid (0.98 g, 6.53 mmol), and K_2CO_3 (2.30 g, 16.64 mmol) was degassed under vacuum. 1,4-dioxane (50 mL) was added, and then the mixture was heated at 85 °C for two days. The contents were poured onto ice-cold H_2O and neutralized with HCl (2 mL) to dissolve any remaining K_2CO_3. The precipitate was filtered off, washed with MeOH, and dried to produce a white powder (Scheme S1). FTIR (KBr, cm^{-1}, Figure S1): 3065 (C–H aromatic), 2859 (CH = O), 1697 (C = O), 1609 (C = C). ^{1}H NMR (500 MHz, DMSO-d_6, δ, ppm, Figure S2): 10.087 (s, 4H, CHO), 8.083 (d, 8H, CH aromatic), 7.938 (d, 8H, CH aromatic). ^{13}C NMR (125 MHz, DMSO-d_6, δ, ppm, Figure S3): 192.647, 137.677, 137.274, 136.233, 130.043, 129.493, 113.829. EI-MS *m/z* 500.7 (Figure S5). Anal. Calcd for $C_{32}H_{20}O_4S$: C, 76.78; H, 4.03; S, 6.40; O, 12.78 %. Found: C, 75.42; H, 4.12; S, 6.83; O, 13.64 %.

2.2.3. Synthesis of 1,3,6,8-Tetra(4-formylphenyl)pyrene (Py-Ph-CHO)

A mixture of Py-4Br (0.54 g, 1.1 mmol), $Pd(PPh_3)_4$ (0.06 g, 0.05 mmol), 4-formylphenylboronic acid (0.98 g, 6.53 mmol), and K_2CO_3 (2.30 g, 16.64 mmol) was degassed under vacuum. 1,4-dioxane (50 mL) was added, and then the mixture was heated at 85 °C for two days. The contents were poured onto ice-cold H_2O and neutralized with HCl (2 mL) to dissolve any remaining K_2CO_3. The precipitate was filtered off, washed with MeOH, and dried to produce a yellow powder (Scheme S2). FTIR (KBr, cm^{-1}, Figure S1): 3041 (CH aromatic), 2813, 2727 (CH = O), 1693 (C = O), 1606 (C = C). HR-FD-MS: *m/z*: 619.185 (Figure S6). Anal. Calcd for $C_{44}H_{26}O_4$: C, 85.42; H, 4.24; O, 10.34 %. Found: C, 85.67; H, 4.18; O, 11.02 %.

2.2.4. Synthesis of 3,3́,5,5́-Tetrabromo-4,4́-biphenol (Bi-4Br-OH)

A solution of 4,4́-biphenol (2.00 g, 10.8 mmol) in MeOH (80 mL) was stirred in an ice-water bather for 1 h until the temperature reached 0 °C. Br_2 (2.76 mL, 53.7 mmol) was added dropwise to the solution, and then the mixture was left at room temperature for 3 h with stirring. The solid precipitate was filtered off and washed sequentially with aqueous $NaHCO_3$ and H_2O. The white solid was dried at 60 °C for 24 h (Scheme S3). FTIR (KBr, cm^{-1}, Figure S7): 3439 (O–H stretching), 3061 (C–H aromatic), 747 (C–Br). ^{1}H NMR (500 MHz, DMSO-d_6, δ, ppm, Figure S8): 10.053 (s, 2H, OH), 7.865 (s, 4H, CH aromatic). ^{13}C NMR (125 MHz, DMSO-d_6, δ, ppm, Figure S9): 150.285, 131.632, 130.035, 112.481. HR-FD-MS: *m/z*: 501.707 (Figure S10). Anal. Calcd for $C_{12}H_6Br_4O_2$: C, 28.72; H, 1.21; O, 6.38 %. Found: C, 29.16; H, 1.22; O, 6.22 %.

2.2.5. Synthesis of 3,3́,5,5́-tetrabromo-4,4́-dimethoxy-1,1́-biphenyl (Bi-4Br-OCH_3)

A mixture of Bi-4Br-OH (2.0 g, 4.0 mmol), methyl iodide (3.4 g, 24 mmol), and K_2CO_3 (1.7 g, 12 mmol) in acetone (50 mL) was heated at 60 °C for 20 h. The solvent was evaporated, and the residue was added to cold H_2O. The solids were filtered off, washed with H_2O, and dried in an oven at 60 °C for 24 h (Scheme S3). FTIR (KBr, cm^{-1}, Figure S1): 3067 (C–H aromatic), 2946 (C–H aliphatic), 744 (C–Br). ^{1}H NMR (500 MHz, DMSO-d_6, δ, ppm, Figure S8): 8.057 (s, 4H, CH aromatic), 3.830 (s, 6H, OCH_3). ^{13}C NMR (125 MHz, DMSO-d_6, δ, ppm, Figure S9): 153.333, 135.779, 131.149, 118.093, 60.486. HR-FD-MS: *m/z*: 529.736 (Figure S11). Anal. Calcd for $C_{14}H_{10}Br_4O_2$: C, 31.74; H, 1.90; O, 6.04 %. Found: C, 32.10; H, 1.89; O, 5.99 %.

2.2.6. Synthesis of 3,3́,5,5́-Tetra(4-formylphenyl)-4,4́-dimethoxybiphenyl (Bi-Ph-CHO)

A mixture of Bi-4Br-OCH_3 (0.54 g, 1.0 mmol), $Pd(PPh_3)_4$ (0.06 g, 0.05 mmol), 4-formylphenylboronic acid (0.98 g, 6.53 mmol), and K_2CO_3 (2.30 g, 16.64 mmol) was degassed under vacuum. 1,4-dioxane (50 mL) was added, and then the mixture was heated at 85 °C for two days. The contents were poured onto ice-cold H_2O and neutralized with HCl (2 mL) to dissolve any remaining K_2CO_3. The precipitate was filtered off, washed with MeOH, and dried to give a white powder (Scheme S3). FTIR (KBr, cm^{-1}, Figure S1): 3067 (C–H aromatic), 2988, 2929 (C–H aliphatic), 2821, 2733 (CH = O), 1689 (C = O), 1610 (C = C). ^{1}H NMR (500 MHz, $CDCl_3$, δ, ppm, Figure S8): 10.087 (s, 4H, CHO), 8.034–7.901 (m, CH aromatic), 3.130 (s, 6H, OCH_3). ^{13}C NMR (125 MHz, $CDCl_3$, δ, ppm, Figure S9): 192.889, 143.831, 135.112, 134.607, 130.086, 129.625, 129.449, 60.713. HR-FD-MS: *m/z*: 630.205 (Figure S12). Anal. Calcd for $C_{42}H_{30}O_6$: C, 79.98; H, 4.79; O, 15.32 %. Found: C, 78.74; H, 4.74; O, 16.06 %.

2.2.7. Synthesis of 1,3,6,8-Tetrakis(4-bromophenyl)pyrene (Py-Ph-Br)

A mixture of Py-4Br (0.10 g, 0.19 mmol), $Pd(PPh_3)_4$ (0.040 g, 0.034 mmol), 4-bromophenylboronic acid (0.18 g, 1.1 mmol), and K_2CO_3 (0.213 g, 1.54 mmol) was degassed under vacuum. 1,4-dioxane (50 mL) was added, and then the mixture was heated at 110 °C for two days. The residue was filtered off and washed with H_2O, THF, and MeOH. The yellow powder was dried for two days at 80 °C (Scheme S4). FTIR (KBr, cm^{-1}, Figure S13): 3027 (C–H aromatic), 1597 (C = C), 676 (C–Br). ^{1}H NMR (500 MHz, DMSO-d_6, δ, ppm, Figure S14): 8.25 (s, 1H), 8.13 (d, 2H), 7.96 (d, 1H), 7.9 (d, 2H), 7.86–7.74 (m, 5H), 7.74–7.75 (m, 6H), 7.51–7.42 (m, 2H), 7.38 (d, 2H). The ^{13}CNMR result of Py-Ph-Br cannot provide due to its poor solubility. HR-FD-MS: *m/z*: 822.90 (Figure S15). Anal. Calcd for $C_{40}H_{22}Br_4$: C, 58.43; H, 2.70 %. Found: C, 57.59; H, 2.80 %.

2.2.8. Synthesis of Ts-ThTh-CMP, Bi-ThTh-CMP, and Py-ThTh-CMP

2,3,4,5-Tetra(4-formylphenyl)thiophene (0.15 g, 0.31 mmol) [or 3,3́,5,5́-tetra(4-formylphenyl)-4,4́-dimethoxybiphenyl (0.15 g, 0.24 mmol) or 1,3,6,8-tetra(4-formylphenyl)pyrene (0.15 g, 0.24 mmol)] and dithiooxamide (0.074 g, 0.61 mmol) were heated at 120 °C in dry DMF (15 mL) for 72 h. The precipitate was filtered off and washed with THF, MeOH, and acetone. The polymer was dried in an oven for two days at 100 °C to afford Ts-ThTh-CMP (or Bi-ThTh-CMP or Py-ThTh-CMP) (Scheme 1). FTIR (KBr, cm^{-1}, Fig. 1**(a)**): 3033 (C–H aromatic), 837 (C–S–C).

2.2.9. Synthesis of Py-PhPh-CMP

A mixture of Py-Ph-Br (0.10 g, 0.12 mmol), 1,4-benzenediboronic acid (0.040 g, 0.24 mmol), K_2CO_3 (0.13 g, 0.96 mmol), and $Pd(PPh_3)_4$ (0.04 g, 0.84 mmol) was heated at 110 °C in DMF (8 mL) and H_2O (2 mL) for 72 h. The precipitate was filtered off and washed sequentially with H_2O, THF, MeOH, and acetone to afford a green solid (Scheme S4). FTIR (KBr, cm^{-1}, Figure S13): 3022 (C–H aromatic), 1607 (C = C).

2.2.10. Photocatalytic hydrogen production

The photocatalytic hydrogen generation experiment was carried out on a photocatalytic reaction cell. 3 mg of CMP powder was added to 10

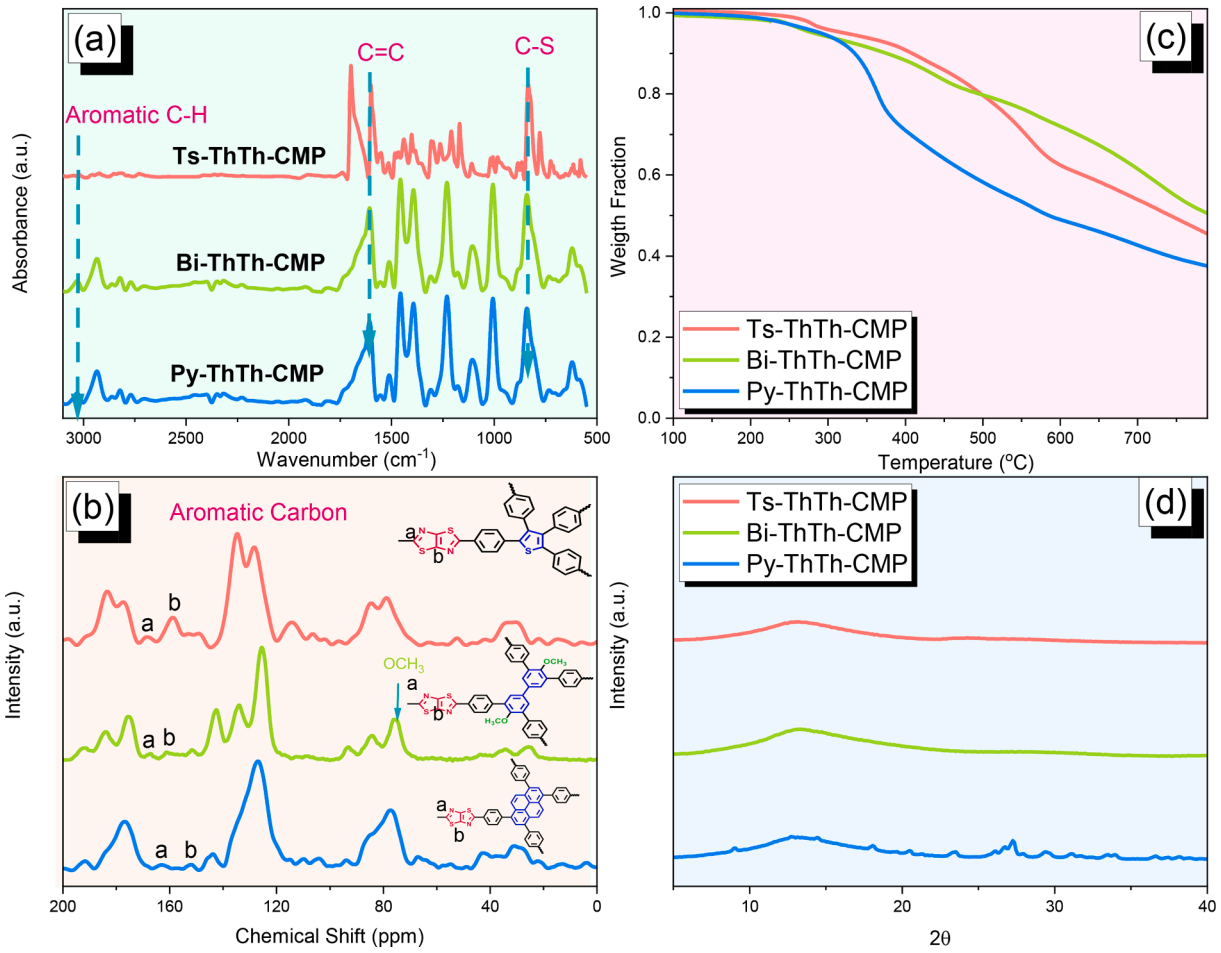

Fig. 1. (a) FTIR spectra, (b) solid-state ^{13}C NMR spectra, (c) TGA analyses, and (d) XRD profiles of Ts-ThTh-CMP, Bi-ThTh-CMP, and Py-ThTh-CMP.

mL (H_2O/MeOH, 4/1, V/V) of 0.1 M aqueous ascorbic acid solution. It was further ultrasonicated for 5 min to obtain a well-dispersed suspension. The resulting suspension was degassed using Argon gas for 10 min to ensure complete air removal prior to irradiation with a 350 W Xe light source (1000 W m − 2; λ > 420 nm) under stirring. The reaction time was 4 h at ambient temperature by a stream of cold water. Ensuring of H_2 production was thermally detected via bit injection by semi-capillary column (molecular sieve; diameter: 8 mm; length: 3 m) into the reactor headspace gas (0.5 μL) into gas chromatography (GC7920) under isothermal parameters. The apparent quantum yield (AQY) was calculated using the following equations:

$$AQY = \frac{number of evolved H_2 molecules \times 2}{number of incident photons} = \frac{N_e}{N_P} = \frac{2M \times N_A}{\frac{E_{total}}{E_{photon}}} = \frac{2M \times N_A}{\frac{S \times P \times t}{h \times \frac{c}{\lambda}}}$$

$$= \frac{2M \times N_A \times h \times c}{S \times P \times t \times \lambda} \times 100\%$$

where N_A is the Avogadro constant, M is the amount of H_2 produced (mol), c is the speed of light, h is the Planck constant, S is the irradiation area (cm^2), t is the photoreaction time (s), P is the intensity of the irradiating light (W cm^{-2}), and λ is the wavelength of the monochromatic light (m).

3. Results and discussion

3.1. Synthesis and characterization of Ts-ThTh-CMP, Bi-ThTh-CMP, and Py-ThTh-CMP

Three CMPs incorporating ThTh moieties were rationally fabricated to function as photocatalysts through the condensation of dithiooxamide with three different aromatic aldehydes (Ts-Ph-CHO, Bi-Ph-CHO, and Py-Ph-CHO, respectively) in DMF at 120 °C for 3 days. These three ThTh-CMPs were insoluble in almost all organic solvents. For example, we checked the solubility of Py-ThTh-CMP in various organic solvents such as acetone, ethanol, THF, DMF and $CHCl_3$, as shown in **Figure S16**. The images showed that Py-ThTh-CMP could not dissolve in all these organic solvents, indicating that Py-ThTh-CMP had a highly crosslinked structure with a high degree of polymerization. These three ThTh-CMPs possessed distinct colors arising from the presence of heteroatoms (S and N) in their different chemical composition (Scheme 1). To confirm the preparation of the three ThTh-CMPs, we recorded their FTIR and solid-state ^{13}C NMR spectra. To ensure the preparation of the three ThTh-CMPs, we recorded their FT-IR and solid-state ^{13}C NMR spectra. The FTIR spectra of the ThTh-CMPs [Fig. 1**(a)**] featured an absorption band near 1685 cm^{-1}, representing unreacted aldehyde groups that are characterized by the appearance of C = O band in the FTIR spectrum of Ts-Ph-CHO, Bi-Ph-CHO, and Py-Ph-CHO [**Figure S1**], which overlapped with a band near 1654 cm^{-1}, representing the (C = N) stretching vibrations of the ThTh moieties. In addition, an intense peak appeared at 840 cm^{-1}, related to C–S bonds that disappeared in the FTIR spectrum of the monomers [**Figure S1**], confirming the incorporation of ThTh units into our three CMPs. The solid-state ^{13}C NMR spectra [Fig. 1**(b)**] of the three ThTh-CMPs featured signals at 167 and 157 ppm representing the sp^2-hybridized carbon atoms of the C = N and C = C units in the ThTh moieties. An additional peak observed at 148 ppm was related to the aromatic carbon atoms attached to the thiazole units. The broad signals from 126 to 135 ppm represent the aromatic carbon atoms in ThTh-CMP structures. For Bi-ThTh-CMP, peaks at 73 and 143 ppm represented the

MeO groups and the aromatic carbon atoms bonded to the MeO units. The solid-state ^{13}C NMR spectrum [**Figure S17**] of the Py-PhPh-CMP featured signals from 139 and 125 ppm representing the aromatic carbon atoms in the Py-PhPh-CMP framework. We performed thermogravimetric analysis (TGA) [Fig. 1**(c)**, Table 1] under N_2 to study the thermal stabilities of our three ThTh-CMPs. The decomposition temperatures at which the weight loss of 5% and 10% (T_{d5} and T_{d10}) were 322 and 408 °C for Ts-ThTh-CMP, 282 and 375 °C for Bi-ThTh-CMP, 291 and 334 °C for Py-ThTh-CMP, 401 and 468 °C for Py-PhPh-CMP [**Figure S18**], respectively, with char residues of 45, 50, 38 and 65 wt %, respectively. In addition, the significant weights loss is also seen in the TGA curves of ThTh-CMPs, which are attributed to the release of some small gaseous molecules or entrapped solvent in their porous structures. X-ray diffraction (XRD) patterns [Fig. 1**(d) and Figure S19**] of the Ts-ThTh-CMP, Bi-ThTh- CMP and Py-PhPh-CMP featured no distinct peak, revealing their amorphous properties. While XRD profile of Py-ThTh-CMP featured some distinct peaks, indicating its semi-crystalline character.

We examined the porous properties of the ThTh-CMPs through N_2 sorption measurements at 77 K [Fig. 2**(a–c) and Figure S20**]. The specific BET surface areas for Ts-ThTh-CMP, Bi-ThTh-CMP, Py-ThTh-CMP, and Py-PhPh-CMP were 70, 316, 125, and 100 $m^2\ g^{-1}$, respectively; the total pore volumes, calculated from the amount of N_2 gas adsorbed when P/P_0 was equal to 0.99, were 0.103, 0.678, and 0.795 $cm^3\ g^{-1}$, respectively. We applied nonlocal density functional theory to estimate the pore sizes of these ThTh-CMPs and Py-PhPh-CMP. Fig. 2 **(d–f)** reveal that all three of the ThTh-CMPs contained micropores and mesopores in their structures, with pore sizes in the range of 2.03–2.30 nm. While the pore size of Py-PhPh-CMP was centered at 1.90 nm as depicted in **Figure S20**. We used SEM and TEM to observe the surface properties of the ThTh-CMPs. The SEM images in Fig. 2**(g–i)** reveal that the surfaces of Ts-ThTh-CMP and Bi-ThTh-CMP both featured the stacking of small particles, whereas a rodlike morphology appeared on the surface of Py-ThTh-CMP. The TEM images of the ThTh-CMPs in Fig. 2**(j–l)** and **Figure S21** revealed layered structures consistent with the SEM images. The SEM images [**Figure S22**] of Py-PhPh-CMP showed aggregation of small spheres and TEM images [**Figure S22**] confirmed its microporosity. Elemental mapping of TEM and SEM confirmed the presence of C, N, O, S, and Pd atoms in ThTh-CMPs materials (**Figures S23- S28**).

3.2. Photoelectronic properties of Ts-ThTh-CMP, Bi-ThTh-CMP, and Py-ThTh-CMP

We used ultraviolet/visible diffuse reflectance spectroscopy (UV–Vis DRS), ultraviolet photoelectron spectroscopy (UPS), steady-state PL spectroscopy, time-correlated single-photon counting (TCSPC), photocurrent measurements, and electrochemical impedance spectroscopy (EIS) to investigate the photoelectronic properties of Ts-ThTh-CMP, Bi-ThTh-CMP, and Py-ThTh-CMP as D–A systems and of Py-PhPh-CMP as a non-D–A system. Fig. 3**(a)** presents the UV–Vis DRS spectra of the three CMPs incorporating the ThTh moieties; they displayed their strongest absorptions in the UV–Vis region. These absorptions extended to 800 nm. Ts-ThTh-CMP, Bi-ThTh-CMP, and Py-ThTh-CMP exhibited absorption bands at 441, 413, and 460 nm. The signal for Py-ThTh-CMP was red-shifted concerning those of the other D–A CMPs. Py-PhPh-CMP provided its most robust band at 390 nm, suggesting that integration of the ThTh moieties in the pyrene-CMP resulted in a severe red-shift (460 nm) as a result of the D–A system and the novel electronic structure. We calculated the band gaps of Ts-ThTh-CMP, Bi-ThTh-CMP, Py-ThTh-CMP, and Py-PhPh-CMP to be 2.0, 2.1, 1.94, and 2.51 eV, respectively [Fig. 3**(b)**]. The bandgap of Py-ThTh-CMP was narrower than those of the other CMPs, suggesting that it might catalyze the reduction of H_2O to H_2 in an effective manner (Table 2). The bandgap of Ts-ThTh-CMP is less than Py-PhPh-CMP and Bi-ThTh-CMP according to a thiophene ring which increases the sulfur content in the CMP backbone and reduces the bandgap of Ts-ThTh-CMP respect to the Py-PhPh-CMP and Bi-ThTh-CMP [68,69]. The presence of D–A systems can result in faster intramolecular charge transfer, highly extended conjugation, and more absorbed light [70]. We used UPS to investigate the band gaps of these CMPs [Fig. 3**(c)**]. The relative valance band maximum (VBM) and the energies (E_{CB}) of the conduction band minimum (CBM) for Ts-ThTh-CMP, Bi-ThTh-CMP, Py-ThTh-CMP, and Py-PhPh-CMP were –5.93/–3.93, –5.61/–3.51, –5.74/–3.80, and –5.74/–3.23, respectively [Fig. 3 **(c)**, **Figure S29**, Table 2]. Because the values of E_{CB} for all of the CMPs were greater than the reduction potential for H_2, these catalysts would have the ability to split H_2O to give H_2. Besides, we consider the Ts-ThTh-CMP, the best candidate for overall water splitting as depicted in the optical band gap structure diagram under visible light concerning the others [71,72]. As a result, we plan in the future work to construct new materials based on the Ts-ThTh-CMPs derivatives and study in detail the overall water splitting under visible light. Moreover, these catalysts could also be used for the reduction of O_2 [62].

The steady-state PL spectra of the as-prepared CMPs featured different fluorescence emission bands and intensities when excited at a wavelength of 350 nm [Fig. 4**(a), Figure S30**]. The emission intensity of the signal from Py-ThTh-CMP was lower than those from the other as-prepared samples; furthermore, it was shifted bathochromically compared with those of Bi-ThTh-CMP and Ts-ThTh-CMP. Thus, we expected the photocatalytic activity of Py-ThTh-CMP to be higher than those of the other two ThTh-CMPs and Py-PhPh-CMP (without ThTh moiety, **Figure S30**) because of its efficiency at generating light-induced charge carriers, its suppression of photogenerated exciton recombination, and its continuous heterojunction, all of which would enhance the charge diffusion rate at the Py–ThTh interfaces [62,73]. To examine the photoelectric properties of the CMPs, we used TCSPC to record their PL decays upon excitation at 450 nm, with observation at 650 nm. Fig. 4**(b)** and **Table S1** reveal that the PL intensities featured fast decay singlet S1 (τ_1 = 0.4887–2.075 ns) and slow decay triplet T1 (τ_2 = 0.08753–0.4938 ns) components. The average lifetimes (τ) of the as-prepared CMPs ranged from 0.2141 to 0.6348 ns. Among our samples, Py-ThTh-CMP afforded a slower PL lifetime. As a result, we suspected that the longer lifetimes for exciton diffusion at the Py–ThTh heterojunctions inhibited nonradiative recombination and that extended electron delocalization through the D–A system extended the lifetime [52] [Fig. 4**(b)**]. Efficient charge separation in the Py-ThTh-CMP was accomplished due to its longer lifetime extension, thereby facilitating H_2 production without any co-catalysts. The photocurrents measured for Ts-ThTh-CMP, Bi-ThTh-CMP, Py-ThTh-CMP, and Py-PhPh-CMP were 2, 0.425, 2, and 0.27 μA cm^{-2} [Fig. 4**(c)**]. The photocurrent measurement revealed that Py-ThTh-CMP and Ts-ThTh-CMP have a stronger photocurrent response than the other in comparison with the others (Fig. 4**c**), indicating that more light-induced excitons in Py-ThTh-CMP are available for the photocatalytic reaction, which is beneficial for the photocatalytic hydrogen evolution. These results revealed that the physical properties and the electronic structures of the Py-ThTh-CMP could be effectively tuned by altering the chemical components and exhibited excellent intramolecular charge transfer for photogenerated electrons, which gives the highest value for H_2 evolution of the Py-ThTh-CMP sample

Table 1
TGA and BET data of Ts-ThTh-CMP, Bi-ThTh-CMP, and Py-ThTh-CMP.

Sample	T_{d5} (°C)	T_{d10} (°C)	Char yield (wt%)	Surface area ($m^2\ g^{-1}$)	Pore size (nm)
Ts-ThTh-CMP	322	408	45	70	2.03
Bi-ThTh-CMP	282	375	50	316	2.07
Py-ThTh-CMP	291	334	38	125	2.30
Py-PhPh-CMP	401	468	65	100	1.90

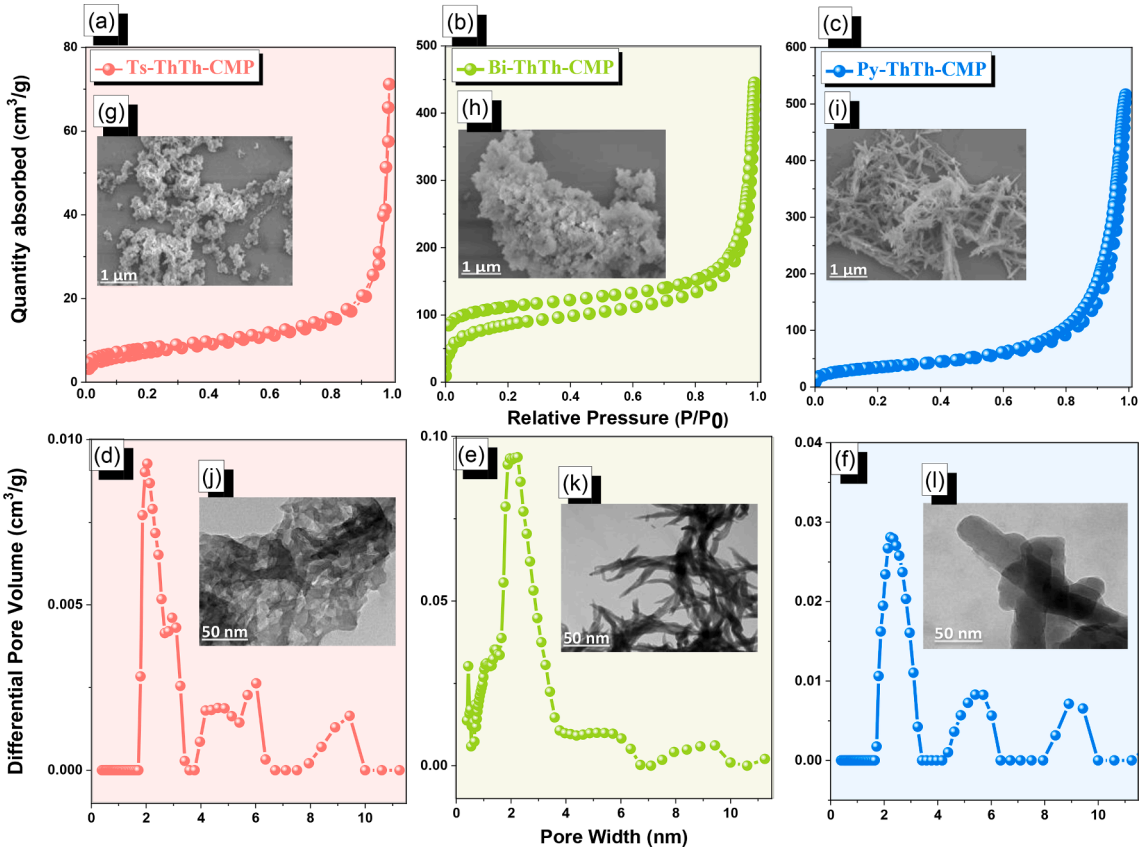

Fig. 2. (a–c) N_2 sorption isotherms, (d–f) pore size distribution curves using nonlocal density functional theory, (g–i) SEM images, and (j–l) TEM images of (a, d, g, j) Ts-ThTh-CMP, (b, e, h, k) Bi-ThTh-CMP, and (c, f, i, l) Py-ThTh-CMP.

[74]. However, Ts-ThTh-CMP gives a high photocurrent response, but the photocatalytic performance is low compared with Py-ThTh-CMP. The Py-ThTh-CMP comprises a strong acceptor (ThTh) with a strong donor (pyrene). In contrast, Ts-ThTh-CMP forms a strong acceptor (ThTh) with a weak donor (thiophene). The Nyquist plot of Py-ThTh-CMP featured a semicircle having a much smaller diameter than the other CMPs, confirming its fastest interfacial charge transfer to facilitate and enhance the photocatalytic activity [75], as outlined in Fig. 4**(d)**. Notably, the Py-PhPh-CMP shows low resistance concerning the Ts-ThTh-CMP and Bi-ThTh-CMP according to the high planarity of pyrene CMP, which contributes to the charge also transfer the presence of Pd, which is loaded with a high amount on the surface of the polymer. All of the previous measurements were consistent with the H_2 evolution rates (HERs) of the CMPs (Table 2).

3.3. Photocatalytic H_2 evolution of Ts-ThTh-CMP, Bi-ThTh-CMP, Py-ThTh-CMP, and Py-PhPh-CMP

We used a Xe lamp ($\lambda < 420$ nm) as a light source to measure the photocatalytic H_2 production over the as-prepared CMPs. Generally, we dispersed 3 mg of each CMP powder in 10 mL of H_2O/MeOH (4:1, v/v) and adjusted the concentration of AA (used as the SED) to 0.1 M. We selected AA as the SED for these CMPs from a study of several other sacrificial reagents, including triethanolamine (TEOA), triethylamine (TEA), and benzyl alcohol (BA) [Fig. 5**(a)**]; the highest HER occurred in the presence of AA [66]. The optimal AA concentration (0.1 M) for the photocatalytic reaction was selected compared with 0.05 and 0.2 M [**Figure S31**]. All the as-prepared CMPs incorporating ThTh moieties could reduce H_2O to H_2 in the presence of visible light ($\lambda > 420$ nm) through the photocatalytic process [Fig. 3**(b)**]. Py-ThTh-CMP, as a material, evolved a moderate amount of H_2 during the first hour. Notably, in second hour, the HER reached a maximum of 1874 µmol $g^{-1}h^{-1}$ and a value superior to those obtained for many reported materials featuring molecular Ni and metallic Pt co-catalysts: TPDTz-COF/Ni (941 µmol $g^{-1}h^{-1}$) [63], amorphous carbon/g-C_3N_4/Pt (747 µmol $g^{-1}h^{-1}$) [76], Carbon@g-Graphene/C3N4/Pt (1.0 wt%) (451 µmol $g^{-1}h^{-1}$) [77], three-dimensional g-C_3N_4/C nanosheets/Pt (1610 µmol $g^{-1}h^{-1}$) [78], CP-CMP10 (150 µmol $g^{-1}h^{-1}$) [20], DBTD-CMP2 (188 µmol $g^{-1}h^{-1}$) [52], CMP9/Pt (96.5 µmol $g^{-1}h^{-1}$) [75], Ta-CMP (478 µmol $g^{-1}h^{-1}$) [79], PyBT-2/Pt (1060 µmol $g^{-1}h^{-1}$) [80], and TP-BDDA/Pt (324 µmol $g^{-1}h^{-1}$) [81]. **Table S2** compares the HER efficiencies of various reported materials. The HERs of Ts-ThTh-CMP (269 µmol $g^{-1}h^{-1}$) and Bi-ThTh-CMP (404 µmol $g^{-1}h^{-1}$) were lower than that of Py-ThTh-CMP (507 µmol $g^{-1}h^{-1}$) because the latter featured Py donor moieties, which ensured excellent separation of photogenerated holes and electrons during the photocatalytic reaction, a more extended conjugated structure, strong absorption in the visible region, and strong interactions between the π orbitals of the Py donor and ThTh acceptor units [51,59,82]. Many CMPs photocatalysts reported previously have contained residual Pd-catalysts that played a critical role in enhancing their HERs [83–86]. All as-prepared CMPs with acceptor bridge showed the presence of residual Pd-catalyst, which integrated from Suzuki – Miyaura coupling reaction in the preparation step of used monomers (**Figure S1-S3**); besides, the pyrene-CMP without acceptor moiety (Py-PhPh-CMP) as outlined in **Figure S4**. Notably, ICP-OES measurements proven the presence of Pd-residual in as-prepared materials was estimated to be 0.105 (Py-ThTh-CMP), 0.0801 (Bi-ThTh-CMP), 0.012 (Ts-ThTh-CMP), and 1.34 wt% (Py-PhPh-CMP), respectively, (**Table S3**). A signal is also detected for Pd-nanoparticles in TEM and SEM images and their EDS diagrams (**Figures S23-S28**). Furthermore, this approves that the role of detected traces of Pd in our compounds is not trivial for HER efficiency. Still, we don't attribute the higher HER efficiency of our

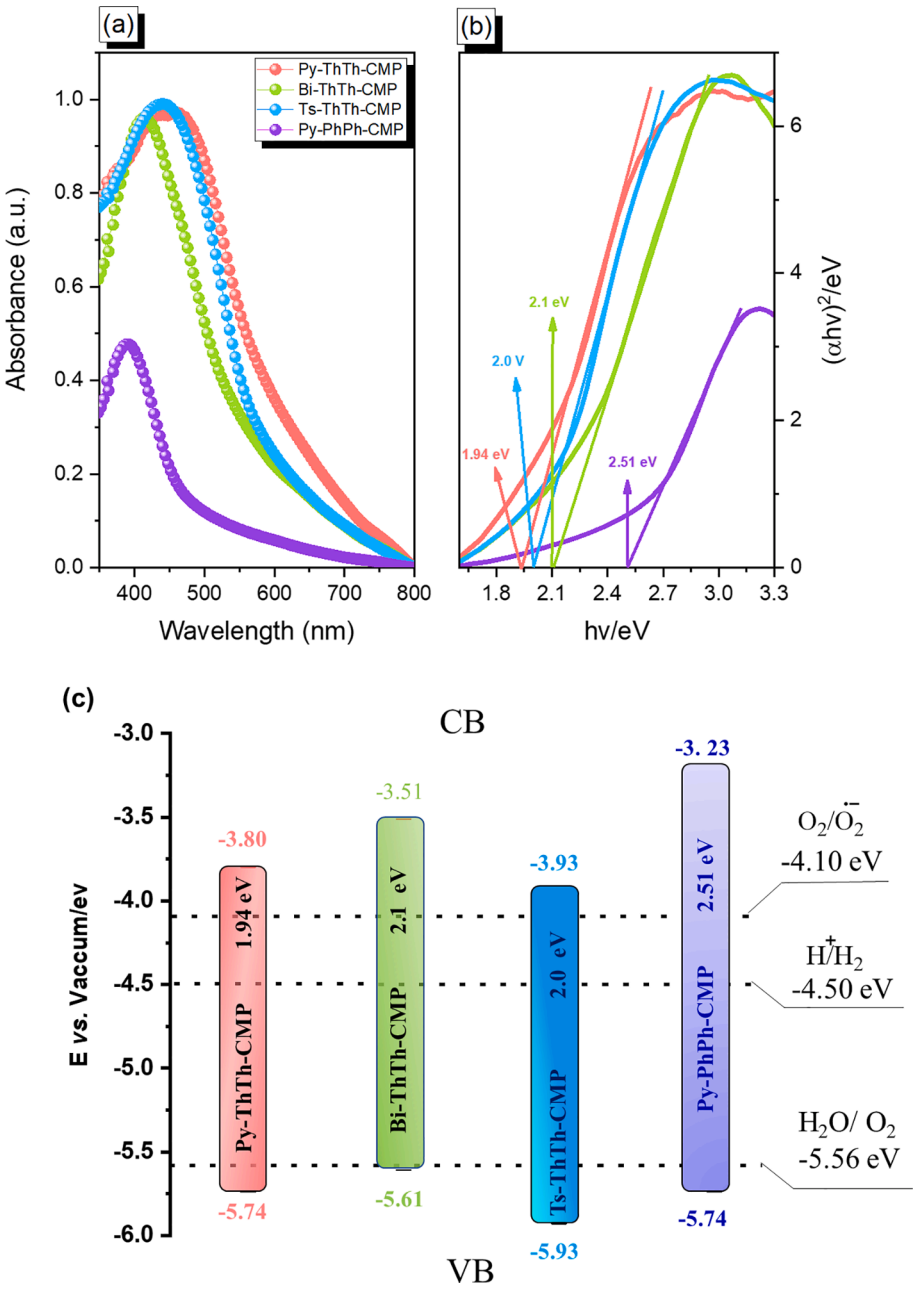

Fig. 3. (a) Diffuse reflectance UV–Vis spectra, (b) Tauc plots of Ts-ThTh-CMP, Bi-ThTh-CMP, Py-ThTh-CMP, and Py-PhPh-CMP and (c) band diagram of Py-ThTh-CMP, Bi-ThTh-CMP, Ts-ThTh-CMP, and Py-PhPh-CMP and their thermodynamic equilibrium redox potentials for O_2 and proton reduction and H_2O oxidation in vacuum scale.

Table 2
Photophysical Properties and HERs of the Four CMPs.

CMP	HOMO/LUMO (eV) [a]	Absorption peak (nm)[b]	Optical gap (eV)[c]	HER (μmol $g^{-1}h^{-1}$)[d]	AQY (%)[e]		
					420 nm	460 nm	500 nm
Ts-ThTh-CMP	–5.93/–3.93	441	2.0	279	0.5	0.25	0.21
Bi-ThTh-CMP	–5.61/–3.51	413	2.1	404	0.11	–	–
Py-ThTh-CMP	–5.74/–3.80	460	1.94	1874	3.4	0.52	0.4
Py-PhPh-CMP	–5.74/–3.23	390	2.51	507	–	–	–

[a] HOMOs was determined using photoelectron spectroscopy; LUMOs derived from the expression $E_{HOMO} - E_g$. [b]Absorption peaks from UV–Vis DRS spectra. [c]Band gaps calculated from Tauc plots. [d]Conditions: 3 mg of CMP in 10 mL of a mixture of H_2O/MeOH (4:1)/0.1 M AA, measured under 350-W Xe light (AM 1.5; λ = 380–780 nm; 1000 W m^{-2}). [e]AQYs measured at 420, 460, and 500 nm.

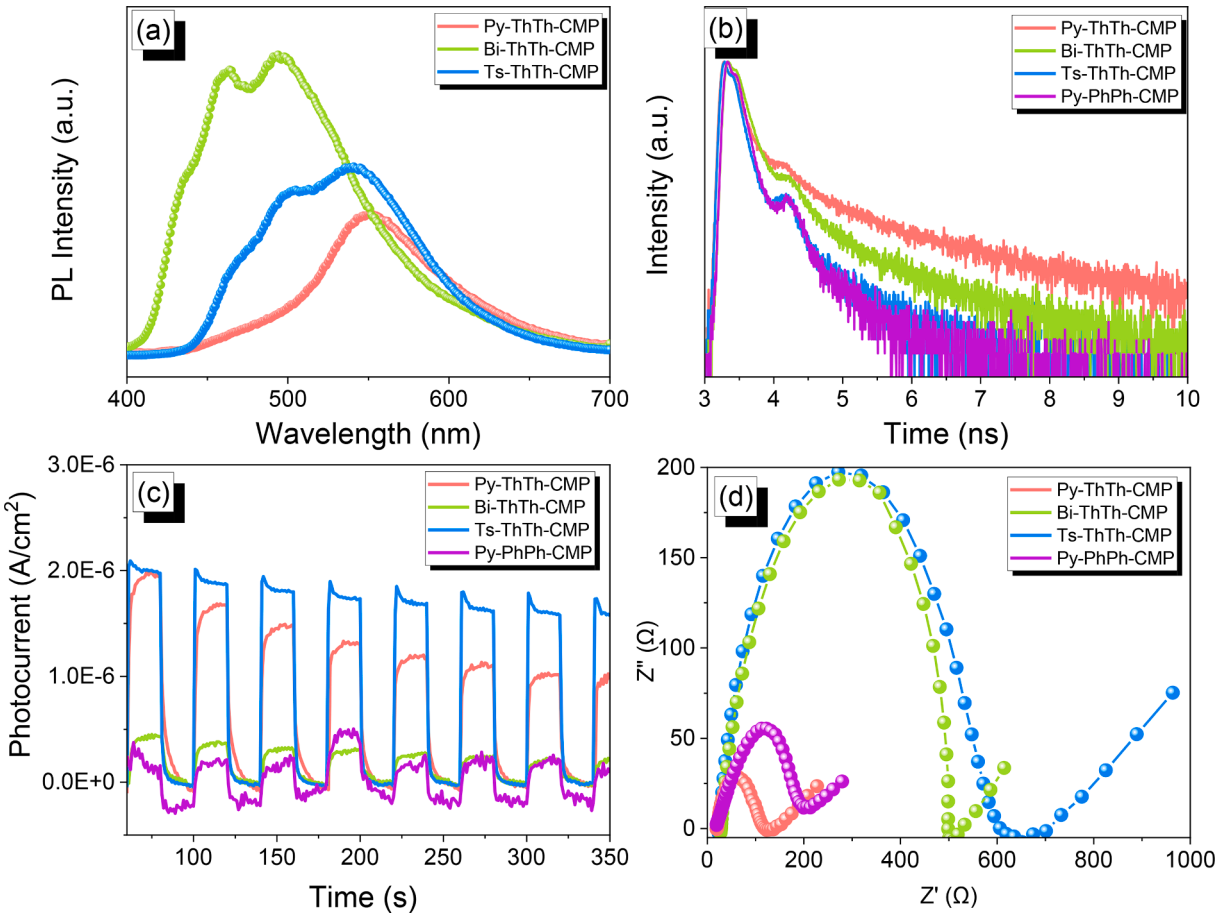

Fig. 4. (a) PL emission spectra of Py-ThTh-CMP, Bi-ThTh-CMP, and Ts-ThTh-CMP in *N*-methyl pyrrolidine; excitation wavelength: 350 nm. (b) TCSPC spectra of the CMPs. (c) Photocurrent curves and (d) Nyquist plots of the CMPs, measured at 2 V vs. Ag/AgCl electrode under light irradiation (LED lamp; $\lambda > 420$ nm) in 0.5 M Na_2SO_4 as the electrolyte. Inset: Equivalent circuit of the electrochemical cell.

prepared CMPs to the presence of Pd-catalyzed residual only. Still, we may attribute it to other reasons, including the optical gap and electronic structure of the D-A system, especially in the case of Py-ThTh-CMP. On the other hand, HER for Py-PhPh-CMP With highly loaded Pd-residual (13400 ppm) with respect to the others equal 507 μmol $g^{-1}h^{-1}$. Notably, Kosco et al. [84] reported that the highest loading of Pd-residual for CPs, which affect the HER, reached 1170 ppm and 50000 ppm from Pt as co-catalyst. To confirm this phenomenon, we examined the effect of the most common co-catalyst (H_2PtCl_6) used in the photocatalytic hydrogen evolution process, which was utilized to load the Pt-co-catalyst on the Py-ThTh-CMP with various wt% (1.5, 3, and 5). All wt% of platinum loading revealed no enhancement in hydrogen evolution rate, as depicted in **Figure S32**. The presence of ThTh linkage acts as electron-output sites owing to their strong electron-withdrawing ability, leading to various physical and chemical properties of the prepared CMPs. Hence, it approves that the CMPs with ThTh moiety are effective photocatalysts without any additional metal co-catalyst.

Thus, our present CMPs are photocatalytic systems without the addition of noble metals as co-catalyst for H_2 production from H_2O. We performed many experiments and optimization processes to examine the importance of each component in our photocatalytic H_2 evolution system, namely, the light ($\lambda > 420$ nm), CMP (catalyst), and SED [Fig. 5**(a)** and **Figures S32–S37**]. The absence of any of these components led to no H_2 being observed during the period of the photocatalytic reaction for up to 4 h. Thus, each component played an essential and critical role in the efficiency of the HER in our system. In addition, we tested the effects of three different weights (1.5, 3.0, and 5.0 mg) of the CMPs incorporating the ThTh acceptor moieties. The best weights for H_2 evolution when using Ts-ThTh-CMP, Bi-ThTh-CMP, and Py-ThTh-CMP were 3.0, 1.5, and 3.0 mg, respectively [Fig. 5**(b) and (c)**]. As well, we evaluated the impact of the dosage of the three CMPs photocatalysts (Ts-ThTh-CMP, Bi-ThTh-CMP, and Py-ThTh-CMP) on the photocatalytic activity since previous studies demonstrated that the mass loading of photocatalyst shows a noticeable effect on the photocatalytic performance due to the saturated light absorption after an optimal amount of photocatalyst [87,88]. As depicted in **Figure S33**, the observed HER for Py-ThTh-CMP slightly increased from 1502 to 1874 μmole $g^{-1}h^{-1}$ under Vis-light irradiation, when increasing the dosage from 1.5 to 3 mg. Besides, the HER suddenly decreased from 1874 to 810 μmole $g^{-1}h^{-1}$, When increasing the dosage from 3 to 5 mg. Notably, Ts-ThTh-CMP and Bi-ThTh-CMP give higher HER for 1.5 mg compared to the other dosages (3 and 5 mg) [**Figures S36 and S37**]. Given a fixed HER, a less photocatalyst dosage indicates a higher photocatalyst efficiency. The decreased efficiency for the three CMPs photocatalysts with high mass loading can be explained by the light scattering and the low utilization ratio of active sites of the polymers during the photocatalytic process. High mass loading of CMPs will cause the particle aggregation to form bigger particles and reduce the dispersity of the polymers in the reaction solution, leading to poor light absorption and transmission and a low utilization ratio of active sites in the polymers photocatalysts. As a result, the HER decreases with the increase in the mass loading of the CMPs photocatalysts.

We estimated the apparent quantum yields (AQYs) of these CMPs by applying band-pass filters with specific wavelengths of 420, 460, and 500 nm in combination with monochromatic light. The highest AQY of

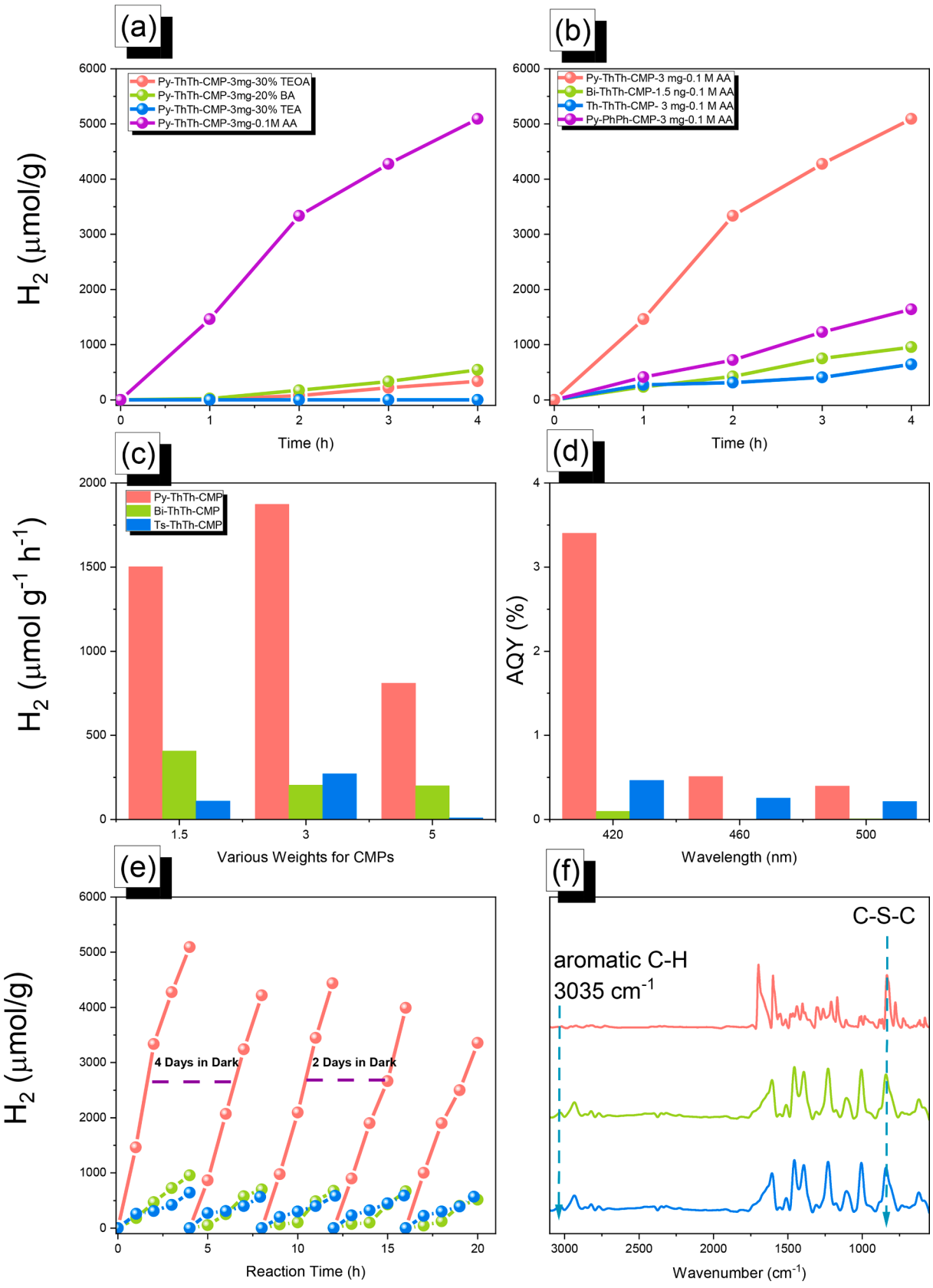

Fig. 5. (a) Optimization of photocatalytic activities for Py-ThTh-CMP using different SEDs. (b) H_2 evolution of Py-ThTh-CMP, Bi-ThTh-CMP, Ts-ThTh-CMP, and Py-PhPh-CMP. (c) HERs of the ThTh-CMPs were measured at different weights. (d) Dependence of the AQY (%) of the H_2 evolution concerning wavelength. (e) Stability and (f) FTIR spectra of Py-ThTh-CMP, Bi-ThTh-CMP, and Ts-ThTh-CMP after the photocatalytic reaction.

3.4% at 420 nm was observed for Py-ThTh-CMP; it decreased to 0.52 and 0.4% at 460 and 500 nm, respectively [Fig. 5**(d)**]. Ts-ThTh-CMP exhibited the same behavior, whereas Bi-ThTh-CMP provided a low AQY at 420 nm and AQYs of zero at 460 and 500 nm. For further confirmation, AQYs for Py-ThTh-CMP with different concentrations (1–4 mg) were taken to give the highest value at 420 nm/3 mg [**Figure S38**]. The Stability experiments performed in the dark with the three new CMPs revealed remarkable recycling through five cycles for Ts-ThTh-CMP and Py-ThTh-CMP and moderate stability for Bi-ThTh-CMP [Fig. 5**(e)**]. For more details, we attempted the stability test of Py-ThTh-CMP via different time intervals in the dark, as depicted in **Figure S39**. The reaction mixture was held after the first run for four days in the dark, and then the stability was slightly decreased in the second and third runs. It was reserved for two days and measured the last two runs (4 and 5) to afford a decrease in the amount of hydrogen evolved compared to two runs (2 and 3). We attributed this decrease to two reasons; the first one for the storage of photocatalyst for a long time in the dark (6 days), and the second reason was the depletion of SED (AA) during the reaction time. We retained the stability test of Py-ThTh-CMP but without storing it in the dark and added the SED (AA) in the second and fourth runs, as shown in **Figure S40**. As a result, we have obtained excellent stability for this CMP. FTIR spectra revealed that none of the CMPs underwent any structural changes during the photocatalytic reactions, confirming the stability of these materials [Fig. 5**(f)**]. Interestingly, the SEM images reveal that the Ts-ThTh-CMP, Bi-ThTh-CMP, and Py-ThTh-CMP preserve their original morphology upon the irradiation process [**Figure S41**]. We have also irradiated the Py-ThTh-CMP upon the exact condition for hydrogen evolution under UV light for 10 h. The FT-IR results showed no noticeable differences between the sample before and after the illumination process outlined in [**Figure S42 (a) and (b)**].

3.4. DFT and TD-DFT calculations for CMPs

For an explanation of the vital role of the absorbed light on the efficiency of H_2 production for prepared compounds at excited states. we estimated the molecular frontier orbitals and the natural transition orbitals (NTOs) via density functional theory (DFT) and time dependent-DFT (TD-DFT) at the B3LYP/6-311G* (d,p) level of theory using Gaussian16 [89]. Upon light absorption, polymers are excited to singlet excited states (Sn), followed by relaxation to the S1 state according to Kasha's rule [90]. Therefore, knowing the S1 excited-state character is crucial to understanding HER photocatalytic activities. As revealed in the natural transition orbitals (NTOs) analysis [Fig. 6], Py-ThTh exhibits a delocalized S1 while Py-PhPh shows a localized π-π* transition on pyrene fragments. On the one hand, the delocalized S1 state explains the smaller optical gap of Py-ThTh as compared to Py-PhPh observed both experimentally and computationally (Fig. 3 **and** Table 3). On the other

Table 3
The computed excitation energy (E_{S_1} *and* E_{T_1} in eV), the energy difference between S1 and T1 (ΔE_{ST} in eV), oscillator strength (f_{S_1} in eV) of the S_1 state at neutral ground state geometry, reorganization energy for electron transfer (λ_e in eV) for the monomer of Py-PhPh and Py-ThTh.

Monomer	E_{S_1}	E_{T1}	ΔE_{ST}	f_{S_1}	λ_e
Py-PhPh	**2.94**	**1.87**	**1.07**	**0.927**	**0.57**
Py-ThTh	**2.55**	**1.83**	**0.72**	**1.381**	**0.43**

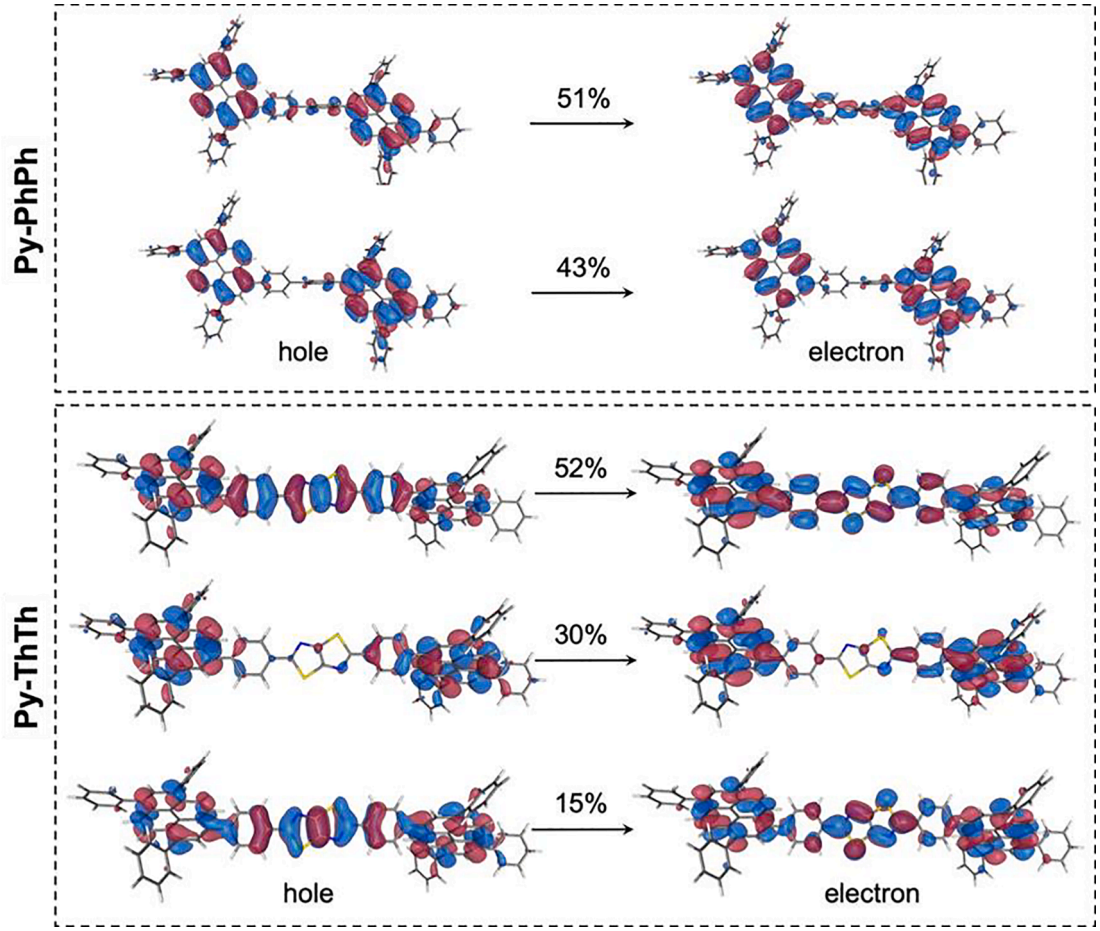

Fig. 6. Natural transition orbitals of the S_1 state of the monomer of Py-PhPh and Py-ThTh (isosurface = 0.05 $Å^{-3}$).

hand, it may explain why Py-ThTh exhibits better HER photocatalytic activity than Py-PhPh. In general, energy transport in polymer *via* delocalized excitons is fast [91,92], which reduces the exciton traveling time to the reaction site where the charge transfer between polymer and sacrificial reagents occurs.

Upon reduction by the sacrificial reagents, the polymer has a negative charge. Fast electron transport within the polymer shortens the electron traveling time to the reaction center for HER, resulting in better photocatalytic activities. Similar to the exciton case, compounds with delocalized LUMO usually exhibit fast electron transport due to small reorganization energy (Table 3) [93–95]. The LUMO of Bi-ThTh and Ts-ThTh is mainly distributed over the central ThTh fragment and two benzene bridges next to it [Fig. 7]. In contrast, the LUMO of Py-PhPh predominantly localizes on the pyrene donor, with a small contribution from the central biphenyl bridge. The LUMO of Py-ThTh delocalizes over nearly the whole molecule. Therefore, we expect Py-ThTh to exhibit faster electron transport than the rest due to LUMO's most considerable degree of spatial delocalization.

To present the role of integration of ThTh linkage in the prepared CMPs backbone. From the literature survey, the small value of the energy difference between singlet state S1 and triplet state T1 (ΔE_{ST}) for the organic materials containing nitrogen enhances the intermolecular charge transfer transition and the spin-orbital coupling effect [96–100]. The smaller ΔE_{ST} value aids the S1 ↔ T1 transfer for excited electrons through intersystem crossing (ISC) and elongates the lifetime of photogenerated electrons in several organic semiconductors [101,102]. These motivated us to study S1 ↔ T1 interaction via TD-DFT of the excited states (S1, T1–T3) for CMPs with and without acceptor (i.e., Py-ThTh-CMP) Py-PhPh-CMP) as summarized in **Tables S4 and S5**. The S1 states of the Py-ThTh exhibit a delocalized S1, which stands for exhibited prominent charge transfer character at singlet state (^{1}CT), while Py-PhPh shows a localized π-π* transition on pyrene fragments [**Figure S43**]. The T1 state of Py-ThTh-CMP showed stronger locally excited triplet states (^{3}LE) characters due to its more planar structure, in which both the holes and the electrons were distributed over it almost entirely. In contrast, The T1 state of Py-PhPh-CMP showed weaker locally excited triplet states (^{3}LE) characters due to the absence of ThTh linkage, in which both the holes and the electrons localized on the pyrene fragment [**Figure S43**]. Moreover, the TD-DFT calculation exhibited a small ΔE_{ST} value for Py-ThTh equal to 0.7211 eV compared to Py-PhPh equal to 1.0704 eV, leading to fast charge separation. Finally, the DFT and TD-DFT calculations revealed that the integration of ThTh moieties for the as-prepared CMPs plays a critical role in hydrogen adsorption and contributes to the photocatalytic H_2O reduction reaction. The mentioned results agree with the experimental results of our UV–Vis-URS, photocurrent, impedance, UPS, TCSPC, and photocatalytic H_2 evolution experiments.

3.5. Photocatalytic mechanism of CMPs with and without ThTh moiety

Fig. 8 displays the mechanism responsible for the promising photocatalytic activities for H_2O reduction when using our CMPs prepared with or without ThTh linkages. We dispersed each target CMP in a mixed solvent of H_2O and MeOH (4:1, v/v), added AA (0.1 M) as the SED, and irradiated the mixture with visible light. The transfer pathways of photogenerated electrons between the electronic energy levels (VBM and CBM) in Py-ThTh-CMP and Py-PhPh-CMP as outlined in Fig. 8. The Py-ThTh-CMP and Py-PhPh-CMP have the same VBM, which sufficiently

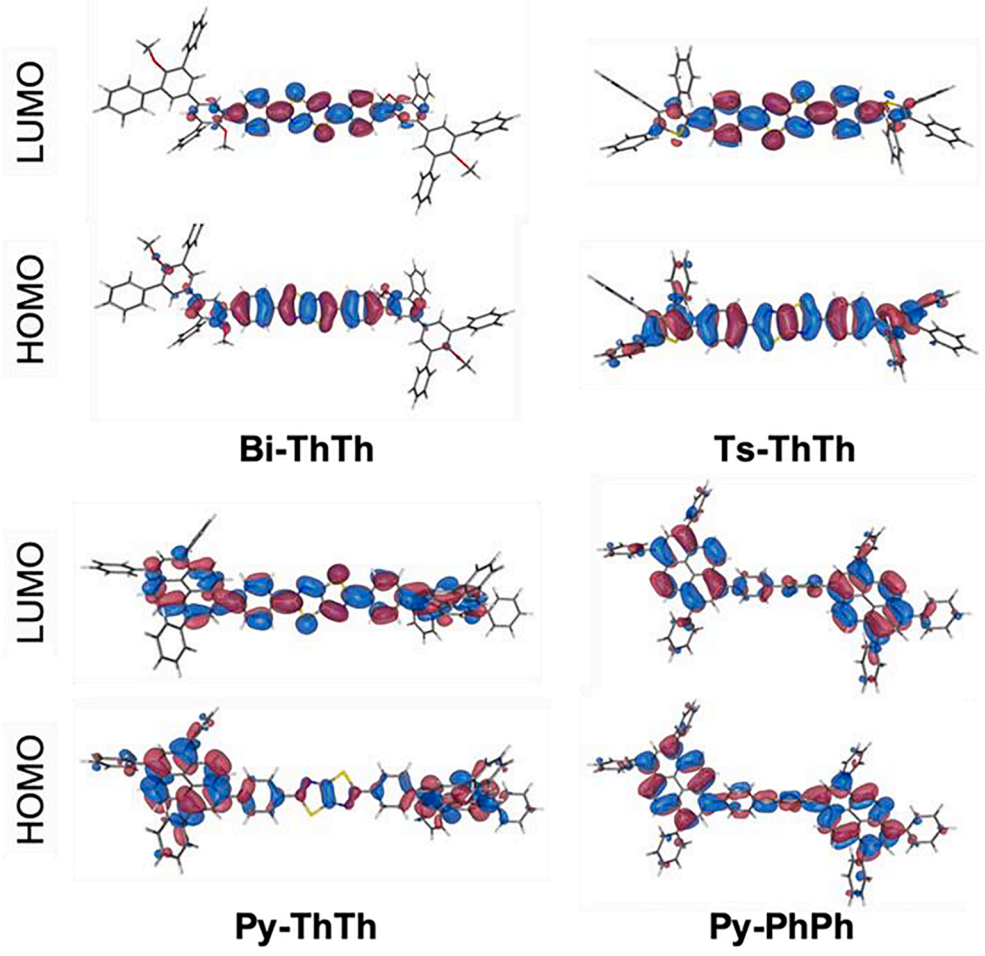

Fig. 7. Frontier orbitals of the monomer of the four CMPs (isosurface = 0.05 Å^{-3}).

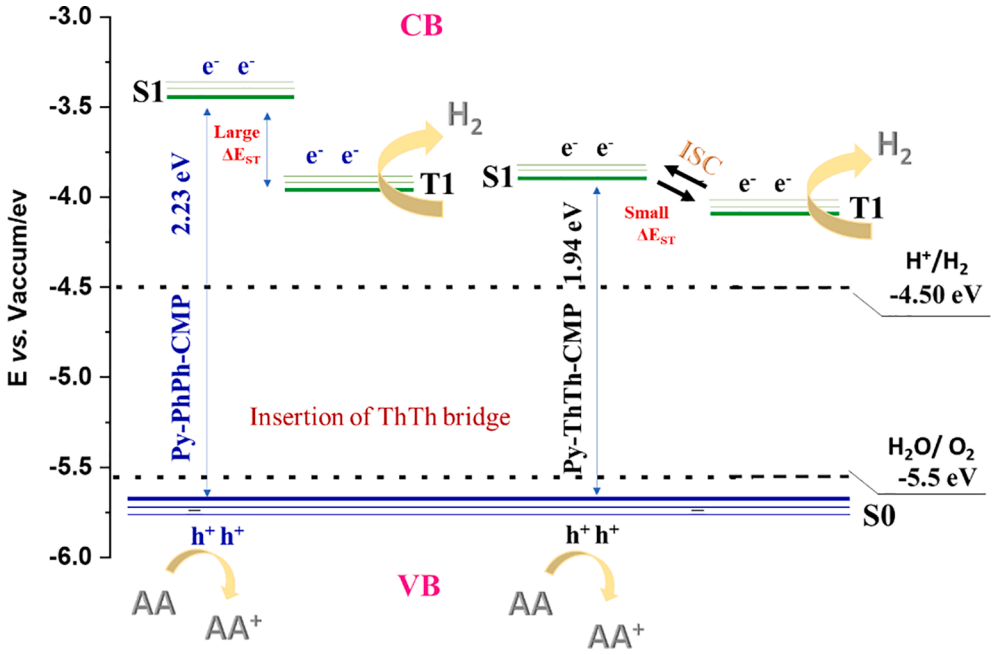

Fig. 8. Schematic representation of the possible photocatalytic mechanism for H_2 evolution over Py-ThTh-CMP and Py-PhPh-CMP.

oxidize the H_2O and different CBM values, which gives a small bandgap in Py-ThTh-CMP and a large one in Py-PhPh-CMP. We calculated the ΔE_{ST} through the excited states (S1 and T1) for these CMPs to give the smaller value in the case of Py-ThTh-CMP, which facilitates the ISC charge transfer while in the absence of acceptor moiety (Py-PhPh-CMP) afford large ΔE_{ST}. As a result, the insertion of the ThTh linkage in the CMPs backbone leads to a smaller bandgap, smaller ΔE_{ST}, and efficient charge separation. The combination of Py and ThTh units created an efficient system for photocatalytic H_2 evolution; when the CMPs containing the ThTh acceptor moieties absorbed light, the excited electrons were delocalized (LUMO), as suggested by the TD-DFT calculations, thereby suppressing the recombination of holes and electrons, with the trapping of holes then being accomplished by AA (as the SED) at the HOMO positions. Furthermore, this combination of donor and acceptor moieties ensured rapid carrier pathways and excellent separation of photogenerated holes and electrons, thereby enhancing the photocatalytic activity relative to that of the CMP prepared without acceptor moieties. Ultimately, the CMPs incorporating ThTh moieties functioned as a robust and excellent system for H_2 production compared with the performance of many previously reported materials, both organic and inorganic.

4. Conclusion

We have prepared three new CMPs incorporating ThTh linkages as D–A systems having the ability to generate H_2 from H_2O under visible light in the presence of AA as the SED without adding any co-catalyst. Notably, Py-ThTh-CMP displayed the highest photocatalytic activity, providing an HER of 1874 μmol $g^{-1}h^{-1}$ because of the high planarity of its Py units, its highly extended conjugation (electron-rich), its strongest absorption in the visible region, its narrowest bandgap, and the strong interactions between the π orbitals of its Py (donor) and ThTh (acceptor) units. Upon light absorption, the TD-DFT calculations revealed the integration of ThTh linkage in prepared CMPs leads to further HOMO/LUMO charge separation, reduces the value of ΔE_{ST}, and accelerates the ISC process. In future studies, we aim to construct new materials based on Ts-ThTh-CMP to simultaneously produce H_2 and O_2 (overall H_2O splitting) under visible light.

Declaration of Competing Interest

The authors declare that they have no known competing financial interests or personal relationships that could have appeared to influence the work reported in this paper.

Acknowledgments

This study was supported financially by the Ministry of Science and Technology, Taiwan, under contracts MOST 108-2638-E-002-003-MY2 and 108-2221-E-110-014-MY3. The authors thank the staff at National Sun Yat-sen University for their assistance with the TEM (ID: EM022600) experiments.

Appendix A. Supplementary data

Supplementary data to this article can be found online at https://doi.org/10.1016/j.cej.2022.137158.

References

[1] Y. Tachibana, L. Vayssieres, J.R. Durrant, Artificial photosynthesis for solar water-splitting, Nat. Photonics. 6 (8) (2012) 511–518, https://doi.org/10.1038/nphoton.2012.175.
[2] J. Zhang, Y. Chen, X.C. Wang, Two-dimensional covalent carbon nitride nanosheets: synthesis, functionalization, and applications, Energy Environ. Sci. 8 (2015) 3092–3108, https://doi.org/10.1039/C5EE01895A.
[3] Z.A. Lan, W. Ren, X. Chen, Y.F. Zhang, X.C. Wang, Conjugated donor-acceptor polymer photocatalysts with electron-output "tentacles" for efficient hydrogen evolution, Appl. Catal., B 245 (2019) 596–603, https://doi.org/10.1016/j.apcatb.2019.01.010.
[4] M. Karayilan, W.P. Brezinski, K.E. Clary, D.L. Lichtenberger, R.S. Glass, J. Pyun, Catalytic metallopolymers from [2Fe-2S] Clusters: artificial metalloenzymes for hydrogen production, Angew. Chem., Int. Ed. 131 (2019) 7617–7630, https://doi.org/10.1002/anie.201813776.
[5] M.H. Elsayed, J. Jayakumar, M. Abdellah, T.H. Mansoure, K. Zheng, A.M. Elewa, C.L. Chang, L.Y. Ting, W.C. Lin, H.H. Yu, W.H. Wang, C.C. Chung, H.H. Chou, Visible-light-driven hydrogen evolution using nitrogen-doped carbon quantum dot-implanted polymer dots as metal-free photocatalysts, Appl. Catal., B 283 (2021), 119659, https://doi.org/10.1016/j.apcatb.2020.119659.
[6] P. Kumar, R. Boukherroub, K. Shankar, Sunlight-driven water-splitting using two-dimensional carbon-based semiconductors, J. Mater. Chem. A 6 (2018) 12876–12931, https://doi.org/10.1039/C8TA02061B.

[7] M.G. Walter, E.L. Warren, J.R. McKone, S.W. Boettcher, Q. Mi, E.A. Santori, N. S. Lewis, Solar water splitting cells, Chem. Rev. 110 (2010) 6446–6473, https://doi.org/10.1021/cr1002326.

[8] L. Cheng, Q. Xiang, Y. Liao, H. Zhang, CdS-Based photocatalysts, Energy Environ. Sci. 11 (2018) 1362–1391, https://doi.org/10.1039/C7EE03640J.

[9] A.F.M. EL-Mahdy, A.M. Elewa, S.-W. Huang, H.-H. Chou, S.-W. Kuo, Dual-function fluorescent covalent organic frameworks: HCl sensing and photocatalytic H_2 evolution from water, Adv. Optical. Mater. 8 (18) (2020) 2000641, https://doi.org/10.1002/adom.202000641.

[10] L.Y. Ting, J. Jayakumar, C.L. Chang, W.C. Lin, M.H. Elsayed, H.H. Chou, Effect of controlling the number of fused rings on polymer photocatalysts for visible-light-driven hydrogen evolution, J. Mater. Chem. A 7 (2019) 22924–22929, https://doi.org/10.1039/C9TA06425G.

[11] X. Chen, S. Shen, L. Guo, S.S. Mao, Semiconductor-based photocatalytic hydrogen generation, Chem. Rev. 110 (2010) 6503–6570, https://doi.org/10.1021/cr1001645.

[12] W.C. Lin, M.H. Elsayed, J. Jayakumar, L.Y. Ting, C.L. Chang, A.M. Elewa, W. S. Wang, C.C. Chung, C.Y. Lu, H.H. Chou, Design and synthesis of cyclometalated iridium-based polymer dots as photocatalysts for visible-light-driven hydrogen evolution, Int. J. Hydrog. Energy 45 (2020) 32072–32081, https://doi.org/10.1016/j.ijhydene.2020.08.288.

[13] R. Asahi, T. Morikawa, H. Irie, T. Ohwaki, Nitrogen-doped titanium dioxide as visible-light-sensitive photocatalyst: designs, developments, and prospects, Chem. Rev. 114 (2014) 9824–9852, https://doi.org/10.1021/cr5000738.

[14] L. Liu, X. Gu, Z. Ji, W. Zou, C. Tang, F. Gao, L. Dong, Anion assisted synthesis of TiO_2 nanocrystals with tunable crystal forms and crystal facets and their photocatalytic redox activities in organic reactions, J. Phys. Chem. C 117 (2013) 18578–18587, https://doi.org/10.1021/jp4064774.

[15] L. Liu, Z. Ji, W. Zou, X. Gu, Y. Deng, F. Gao, C. Tang, L. Dong, In situ loading transition metal oxide clusters on TiO_2 nanosheets as Co-catalysts for exceptional high photoactivity, ACS Catal. 3 (2013) 2052–2061, https://doi.org/10.1021/cs4002755.

[16] W.H. Wang, L.Y. Ting, J. Jayakumar, C.L. Chang, W.C. Lin, C.C. Chung, M. H. Elsayed, C.Y. Lu, A.M. Elewa, H.H. Chou, Design and synthesis of phenylphosphine oxide-based polymer photocatalysts for highly efficient visible-light-driven hydrogen evolution, Sustain. Energy Fuels 4 (2020) 5264–5270, https://doi.org/10.1039/D0SE00928H.

[17] R.S. Sprick, C.M. Aitchison, E. Berardo, L. Turcani, L. Wilbraham, B.M. Alston, K. E. Jelfs, M.A. Zwijnenburg, A.I. Cooper, Maximising the hydrogen evolution activity in organic photocatalysts by co-polymerisation, J. Mater. Chem. A 6 (2018) 11994–12003, https://doi.org/10.1039/C8TA04186E.

[18] M.G. Mohamed, A.F.M. EL-Mahdy, Y. Takashi, S.-W. Kuo, Ultrastable conductive microporous covalent triazine frameworks based on pyrene moieties provide high-performance CO_2 uptake and super capacitance, New J. Chem. 44 (20) (2020) 8241–8253.

[19] X. Feng, Y. Pi, Y. Song, C. Brzezinski, Z. Xu, Z. Li, W. Lin, Metal-organic frameworks significantly enhance photocatalytic hydrogen evolution and CO_2 reduction with earth-abundant copper photosensitizers, J. Am. Chem. Soc. 142 (2020) 690–695, https://doi.org/10.1021/jacs.9b12229.

[20] R.S. Sprick, J.-X. Jiang, B. Bonillo, S. Ren, T. Ratvijitvech, P. Guiglion, M. A. Zwijnenburg, D.J. Adams, A.I. Cooper, Tunable organic photocatalysts for visible-light-driven hydrogen evolution, J. Am. Chem. Soc. 137 (2015) 3265–3270, https://doi.org/10.1021/ja511552k.

[21] J. Wang, G. Ouyang, D. Wang, J. Li, J. Yao, W.S. Li, H. Li, Enhanced photocatalytic performance of donor–acceptor-type polymers based on a thiophene-contained polycyclic aromatic unit, Macromolecules 54 (2021) 2661–2666, https://doi.org/10.1021/acs.macromol.1c00316.

[22] M.G. Mohamed, C.-C. Lee, A.F.M. EL-Mahdy, J. Lüder, M.-H. Yu, Z. Li, Z. Zhu, C.-C. Chueh, S.-W. Kuo, Exploitation of two dimensional conjugated covalent organic frameworks based on tetraphenylethylene with bicarbazole and pyrene units and applications in perovskite solar cells, J. Mater. Chem. A 8 (22) (2020) 11448–11459.

[23] M.G. Mohamed, M.M. Samy, T.H. Mansoure, C.J. Li, W.C. Li, J.H. Chen, K. Zhang, S.W. Kuo, Microporous carbon and carbon/metal composite materials derived from bio-benzoxazine-linked precursor for CO_2 capture and energy storage applications, Int. J. Mol. Sci. 23 (2022) 347, https://doi.org/10.3390/ijms23010347.

[24] J.S.M. Lee, A.I. Cooper, Advances in conjugated microporous polymers, Chem. Rev. 120 (2020) 2171–2214, https://doi.org/10.1021/acs.chemrev.9b00399.

[25] M.M. Samy, M.G. Mohamed, T.H. Mansoure, T.S. Meng, M.A.R. Khan, C.C. Liaw, S.W. Kuo, Solid state chemical transformations through ring-opening polymerization of ferrocene-based conjugated microporous polymers in host–guest complexes with benzoxazine-linked cyclodextrin, J Taiwan Inst. Chem. Eng. 123 (2022), 104110, https://doi.org/10.1016/j.jtice.2021.10.010.

[26] M.G. Mohamed, T.H. Mansoure, Y. Takashi, M.M. Samy, T. Chen, S.W. Kuo, Ultrastable porous organic/inorganic polymers based on polyhedral oligomeric silsesquioxane (POSS) hybrids exhibiting high performance for thermal property and energy storage, Microporous Mesoporous Mater. 328 (2021), 111505, https://doi.org/10.1016/j.micromeso.2021.111505.

[27] S.B. Ren, P.X. Li, A. Stephenson, L.J. Chen, M.E. Briggs, R. Clowes, A. Alahmed, K. K. Li, W.P. Jia, D.M. Han, 1,3-Diyne-linked conjugated microporous polymer for selective CO_2 capture, Ind. Eng. Chem. Res. 57 (2018) 9254–9260, https://doi.org/10.1021/acs.iecr.8b01401.

[28] M.G. Mohamed, T.C. Chen, S.W. Kuo, Solid-state chemical transformations to enhance gas capture in benzoxazine-linked conjugated microporous polymers, Macromolecules 54 (2021) 5866–5877, https://doi.org/10.1021/acs.macromol.1c00736.

[29] M.M. Samy, M.G. Mohamed, A.F.M. El-Mahdy, T.H. Mansoure, K.C.W. Wu, S. W. Kuo, High-performance supercapacitor electrodes prepared from dispersions of tetrabenzonaphthalene-based conjugated microporous polymers and carbon nanotubes, ACS Appl. Mater. Interfaces 13 (2021) 51906–51916, https://doi.org/10.1021/acsami.1c05720.

[30] M.G. Mohamed, A.F.M. EL-Mahdy, M.G. Kotp, S.W. Kuo, Advances in porous organic polymers: syntheses, structures, and diverse applications, Mater. Adv. 3 (2022) 707–733, https://doi.org/10.1039/D1MA00771H.

[31] M.G. Mohamed, M.Y. Tsai, C.F. Wang, C.F. Huang, M. Danko, L. Dai, T. Chen, S. W. Kuo, Multifunctional polyhedral oligomeric silsesquioxane (POSS) based hybrid porous materials for CO_2 uptake and iodine adsorption, Polymers 13 (2021) 221, https://doi.org/10.3390/polym13020221.

[32] M.G. Mohamed, M.M.M. Ahmed, W.T. Du, S.W. Kuo, Meso/microporous carbons from conjugated hyper-crosslinked polymers based on tetraphenylethene for high-performance CO_2 capture and supercapacitor, Molecules 26 (2021) 738, https://doi.org/10.3390/molecules26030738.

[33] M.G. Mohamed, E.C. Atayde Jr, B.M. Matsagar, J. Na, Y. Yamauchi, K.C.W. Wu, S. W. Kuo, Construction hierarchically mesoporous/microporous materials based on block copolymer and covalent organic framework, J. Taiwan Inst. Chem. Eng. 112 (2020) 180–192.

[34] B. Bonillo, R.S. Sprick, A.I. Cooper, Tuning photophysical properties in conjugated microporous polymers by comonomer doping strategies, Chem. Mater. 28 (10) (2016) 3469–3480.

[35] M.G. Mohamed, N.Y. Liu, A.F.M. EL-Mahdy, S.W. Kuo, Ultrastable luminescent hybrid microporous polymers based on polyhedral oligomeric silsesquioxane for CO_2 uptake and metal ion sensing, Microporous Mesoporous Mater. 311 (2021), 110695, https://doi.org/10.1016/j.micromeso.2020.110695.

[36] C. Zhang, Y.u. Qiao, P. Xiong, W. Ma, P. Bai, X. Wang, Q. Li, J. Zhao, Y. Xu, Y. Chen, J.H. Zeng, F. Wang, Y. Xu, J.-X. Jiang, Conjugated microporous polymers with tunable electronic structure for high-performance potassium-ion batteries, ACS Nano 13 (1) (2019) 745–754.

[37] K.I. Aly, M.M. Sayed, M.G. Mohamed, S.W. Kuo, O. Younis, A facile synthetic route and dual function of network luminescent porous polyester and copolyester containing porphyrin moiety for metal ions sensor and dyes adsorption, Microporous Mesoporous Mater. 298 (2020), 110063, https://doi.org/10.1016/j.micromeso.2020.110063.

[38] A.M. Elewa, A.F.M. EL-Mahdy, M.H. Elsayed, M.G. Mohamed, S.W. Kuo, H. H. Chou, Sulfur-doped triazine-conjugated microporous polymers for achieving the robust visible-light-driven hydrogen evolution, Chem. Eng. J. 421 (2021), 129825, https://doi.org/10.1016/j.cej.2021.129825.

[39] P.Y. Ju, S.J. Wu, Q. Su, X.D. Li, Z.Q. Liu, G.H. Li, Q.L. Wu, Salen-porphyrin-based conjugated microporous polymer supported Pd nanoparticles: highly efficient heterogeneous catalysts for aqueous C-C coupling reactions, J. Mater. Chem. A. 7 (2019) 2660–2666, https://doi.org/10.1039/C8TA11330K.

[40] N. Keller, M. Calik, D. Sharapa, H.R. Soni, P.M. Zehetmaier, S. Rager, F. Auras, A. C. Jakowetz, A. Goerling, T. Clark, T. Bein, Enforcing extended porphyrin J-aggregate stacking in covalent organic frameworks, J. Am. Chem. Soc. 140 (2018) 16544–16552, https://doi.org/10.1021/jacs.8b08088.

[41] Y.Y. Dai, W.J. Li, Z.X. Chen, X.G. Zhu, J.L. Liu, R.Y. Zhao, D.S. Wright, A. Noori, M.F. Mousavi, C. Zhang, An air-stable electrochromic conjugated microporous polymer as an emerging electrode material for hybrid energy storage systems, J. Mater. Chem. A. 7 (2019) 16397–16405, https://doi.org/10.1039/C9TA03001H.

[42] M.M. Samy, M.G. Mohamed, S.W. Kuo, Pyrene-functionalized tetraphenylethylene polybenzoxazine for dispersing single-walled carbon nanotubes and energy storage, Compos. Sci. Technol. 199 (2020), 108360, https://doi.org/10.1016/j.compscitech.2020.108360.

[43] W. Zeng, Y. Zhang, X.B. Zhao, M.L. Qin, X.Y. Li, W.S. Jin, D.Q. Zhang, One-pot synthesis of conjugated microporous polymers based on extended molecular graphenes for hydrogen storage, Polymer 174 (2019) 96–100, https://doi.org/10.1016/j.polymer.2019.04.069.

[44] M.G. Mohamed, S.U. Sharma, N.Y. Liu, T.H. Mansoure, M.M. Samy, S. V. Chaganti, Y.L. Chang, J.T. Lee, S.W. Kuo, Ultrastable covalent triazine organic framework based on anthracene moiety as platform for high-performance carbon dioxide adsorption and supercapacitors, Int. J. Mol. Sci. 23 (2022) 3174, https://doi.org/10.3390/ijms23063174.

[45] H.L. Cao, H.B. Huang, Z. Chen, B. Karadeniz, J. Lu, R. Cao, Ultrafine silver nanoparticles supported on a conjugated microporous polymer as high performance nanocatalysts for nitrophenol reduction, ACS Appl. Mater. Interfaces 9 (2017) 5231–5236, https://doi.org/10.1021/acsami.6b13186.

[46] C. Dai, B. Liu, Conjugated polymers for visible-light-driven photocatalysis, Energy Environ. Sci. 13 (2020) 24–52, https://doi.org/10.1039/C9EE01935A.

[47] K. Zhang, D. Kopetzki, P.H. Seeberger, M. Antonietti, F. Vilela, Surface area control and photocatalytic activity of conjugated microporous poly (benzothiadiazole) networks, Angew. Chem. Int. Ed. 52 (2013) 1432–1436, https://doi.org/10.1002/anie.201207163.

[48] F.L. Lai, Y. Wang, D.D. Li, X.S. Sun, J. Peng, X.D. Zhang, Y.P. Tian, T.X. Liu, Visible light-driven superoxide generation by conjugated polymers for organic synthesis, Nano Res. 11 (2018) 1099–1108, https://doi.org/10.1007/s12274-017-1729-6.

[49] Y.Y. Liu, Z.J. Liao, X.L. Ma, Z.H. Xiang, Ultrastable and efficient visible-light driven hydrogen production based on donor-acceptor copolymerized covalent organic polymer, ACS Appl. Mater. Interfaces 10 (2018) 30698–30705, https://doi.org/10.1021/acsami.8b10022.

[50] M.G. Mohamed, M.M. Samy, T.H. Mansoure, S.U. Sharma, M.S. Tsai, J.H. Chen, J. T. Lee, S.W. Kuo, Dispersions of 1,3,4-oxadiazole-linked conjugated microporous polymers with carbon nanotubes as a high-performance electrode for supercapacitors, ACS Appl. Energy Mater. 5 (2022) 3677–3688, https://doi.org/10.1021/acsaem.2c00100.

[51] Z.J. Wang, X.Y. Yang, T.J. Yang, Y.B. Zhao, F. Wang, Y. Chen, J.H. Zeng, C. Yan, F. Huang, J.X. Jiang, Dibenzothiophene dioxide based conjugated microporous polymers for visible-light-driven hydrogen production, ACS Catal. 8 (2018) 8590–8596, https://doi.org/10.1021/acscatal.8b02607.

[52] C. Su, X.G. Duan, J. Miao, Y.J. Zhong, W. Zhou, S.B. Wang, Z.P. Shao, Mixed conducting perovskite materials as superior catalysts for fast aqueous-phase advanced oxidation: a mechanistic study, ACS Catal. 7 (2017) 388–397, https://doi.org/10.1021/acscatal.6b02303.

[53] W.L. Sheng, J.L. Shi, H.M. Hao, X. Li, X.J. Lang, Selective aerobic oxidation of sulfides by cooperative polyimide-titanium dioxide photocatalysis and triethylamine catalysis, J. Colloid Interface Sci. 565 (2020) 614–622, https://doi.org/10.1016/j.jcis.2020.01.046.

[54] R. Li, B.C. Ma, W. Huang, L. Wang, D. Wang, H. Lu, K. Landfester, K.A.I. Zhang, Photocatalytic regioselective and stereoselective [2+2] cycloaddition of styrene derivatives using a heterogeneous organic photocatalyst, ACS Catal. 7 (2017) 3097–3101, https://doi.org/10.1021/acscatal.7b00490.

[55] B.P. Biswal, D. Becker, N. Chandrasekhar, J.S. Seenath, S. Paasch, S. Machill, F. Hennersdorf, E. Brunner, J.J. Weigand, R. Berger, X.L. Feng, Exploration of thiazolo[5,4-d]thiazole linkages in conjugated porous organic polymers for chemoselective molecular sieving, Chem. Eur. J. 24 (2018) 10868–10875, https://doi.org/10.1002/chem.201802631.

[56] M. Samal, S. Valligatla, N.A. Saad, M.V. Rao, D.N. Rao, R. Sahu, B.P. Biswal, A thiazolo[5,4-d]thiazole-bridged porphyrin organic framework as a promising nonlinear optical material, Chem. Commun. 55 (2019) 11025–11028, https://doi.org/10.1039/C9CC05415D.

[57] T.X. Wang, H.P. Liang, D.A. Anito, X.S. Ding, B.H. Han, Emerging applications of porous organic polymers in visible-light photocatalysis, J. Mater. Chem. A. 8 (2020) 7003–7034, https://doi.org/10.1039/D0TA00364F.

[58] Z.X. Gu, Y.J. Chen, Z.X. Wei, L.P. Qian, A.M. Al-Enizi, J.M. Ma, G. Zhou, G. F. Zheng, Precise tuning of heteroatom positions in polycyclic aromatic hydrocarbons for electrocatalytic nitrogen fixation, J. Colloid Interface Sci. 580 (2020) 623–629, https://doi.org/10.1016/j.jcis.2020.07.046.

[59] Y. Wang, H. Liu, Q. Pan, N. Ding, C. Yang, Z. Zhang, C. Jia, Z. Li, J. Liu, Y. Zhao, Construction of Thiazolo[5,4–*d*]thiazole-based two-dimensional network for efficient photocatalytic CO_2 reduction, ACS Appl. Mater. Interfaces 12 (2020) 46483–46489, https://doi.org/10.1021/acsami.0c12173.

[60] Q. Huang, L. Guo, N. Wang, X. Zhu, S. Jin, B. Tan, Layered Thiazolo[5,4–*d*] thiazole-linked conjugated microporous polymers with heteroatom adoption for efficient photocatalysis application, ACS Appl. Mater. Interfaces 11 (2019) 15861–15868, https://doi.org/10.1021/acsami.8b21765.

[61] X. Li, H. Hao, X. Lang, Thiazolo[5,4-d]thiazole linked conjugated microporous polymer photocatalysis for selective aerobic oxidation of amines, J. Colloid Interface Sci. 593 (2021) 380–389, https://doi.org/10.1016/j.jcis.2021.02.111.

[62] W. Li, X. Huang, T. Zeng, Y.A. Liu, W. Hu, H. Yang, Y. Zhang, K. Wen, Thiazolo [5,4- d]thiazole-based donor-acceptor covalent organic framework for sunlight-driven hydrogen evolution, Angew. Chem. Int. Ed. 60 (2021) 1869–1874, https://doi.org/10.1002/anie.202014408.

[63] B.P. Biswal, H.A. Vignolo-Gonzalez, T. Banerjee, L. Grunenberg, G. Savasci, K. Gottschling, J. Nuss, C. Ochsenfeld, B.V. Lotsch, Sustained solar H_2 evolution from a Thiazolo[5,4–d]thiazole-bridged covalent organic framework and nickel-thiolate cluster in water, J. Am. Chem. Soc. 141 (2019) 11082, https://doi.org/10.1021/jacs.9b03243.

[64] A. Hayat, F. Raziq, M. Khan, J. Khan, S. Mane, A. Ahmad, M. Rahman, W. Khan, Fusion of conjugated bicyclic co-polymer within polymeric carbon nitride for high photocatalytic performance, J. Colloid Interface Sci. 554 (2019) 627–639, https://doi.org/10.1016/j.jcis.2019.07.048.

[65] A.F.M. EL-Mahdy, M.G. Mohamed, T.H. Mansoure, H.H. Yu, T. Chen, S.W. Kuo, Ultrastable tetraphenyl-*p*-phenylenediamine-based covalent organic frameworks as platforms for high-performance electrochemical supercapacitors, Chem. Commun. 55 (2019) 14890–14893, https://doi.org/10.1039/C9CC08107K.

[66] M.G. Mohamed, M.H. Elsayed, A.M. Elewa, A.F.M. EL-Mahdy, C.-H. Yang, A.A. K. Mohammed, H.-H. Chou, S.-W. Kuo, Pyrene-containing conjugated organic microporous polymers for photocatalytic hydrogen evolution from water, Catal. Sci. Technol. 11 (6) (2021) 2229–2241, https://doi.org/10.1039/D0CY02482A.

[67] J.X. Jiang, A. Trewin, D.J. Adams, A.I. Cooper, Band gap engineering in fluorescent conjugated microporous polymers, Chem. Sci. 2 (2011) 1777–1781, https://doi.org/10.1039/C1SC00329A.

[68] H. Starukh, P. Praus, Doping of graphitic carbon nitride with non-metal elements and its applications in photocatalysis, Catalysts 10 (2020) 1119, https://doi.org/10.3390/catal10101119.

[69] J. Byun, K.A.I. Zhang, Designing conjugated porous polymers for visible light-driven photocatalytic chemical transformations, Mater. Horiz. 7 (2020) 15–31, https://doi.org/10.1039/C9MH01071H.

[70] K. Lei, D. Wang, L. Ye, M. Kou, Y. Deng, Z. Ma, L. Wang, Y. Kong, A metal-free donor-acceptor covalent organic framework photocatalyst for visible-light-driven reduction of CO_2 with H_2O, ChemSusChem 13 (2020) 1725–1729, https://doi.org/10.1002/cssc.201903545.

[71] Y. Wan, L. Wang, H. Xu, X. Wu, J. Yang, A simple molecular design strategy for two-dimensional covalent organic framework capable of visible-light-driven water splitting, J. Am. Chem. Soc. 142 (2020) 4508–4516, https://doi.org/10.1021/jacs.0c00564.

[72] P. Guiglion, C. Butchosa, M.A. Zwijnenburg, Polymer photocatalysts for water splitting: insights from computational modeling, Macromol. Chem. Phys. 217 (2016) 344–353, https://doi.org/10.1002/macp.201500432.

[73] L. Jiang, X. Yuan, G. Zeng, Z. Wu, J. Liang, X. Chen, L. Leng, H. Wang, H. Wang, Metal-free efficient photocatalyst for stable visible-light photocatalytic degradation of refractory pollutant, Appl. Catal. B Environ. 221 (2018) 715–725, https://doi.org/10.1016/j.apcatb.2017.09.059.

[74] G.B. Wang, F.C. Zhu, Q.Q. Lin, J.L. Kan, K.H. Xie, S. Li, Y. Geng, Y.B. Dong, Rational design of benzodifuran-functionalized donor–acceptor covalent organic frameworks for photocatalytic hydrogen evolution from water, Chem. Commun. 57 (2021) 4464–4467, https://doi.org/10.1039/D1CC00854D.

[75] S. Kandambeth, A. Mallick, B. Lukose, M.V. Mane, T. Heine, R. Banerjee, Construction of crystalline 2D covalent organic frameworks with remarkable chemical (acid/base) stability via a combined reversible and irreversible route, J. Am. Chem. Soc. 134 (2012) 19524–19527, https://doi.org/10.1021/ja308278w.

[76] Q. Xu, B. Cheng, J. Yu, G. Liu, Making co-condensed amorphous carbon/g-C_3N_4 composites with improved visible-light photocatalytic H_2-production performance using Pt as cocatalyst, Carbon 118 (2017) 241–249, https://doi.org/10.1016/j.carbon.2017.03.052.

[77] Q. Xiang, J. Yu, M. Jaroniec, Preparation and enhanced visible-light photocatalytic H_2-production activity of graphene/C_3N_4 composites, J. Phys. Chem. C 115 (2011) 7355–7363, https://doi.org/10.1021/jp200953k.

[78] W. Che, W. Cheng, T. Yao, F. Tang, W. Liu, H. Su, Y. Huang, Q. Liu, J. Liu, F. Hu, Z. Pan, Z. Sun, S. Wei, Fast photoelectron transfer in (Cring)–C_3N_4 plane heterostructural nanosheets for overall water splitting, J. Am. Chem. Soc. 139 (2017) 3021–3026, https://doi.org/10.1021/jacs.6b11878.

[79] K. Ding, Q. Zhang, Q. Li, S. Ren, Terminal group effect of conjugated microporous polymers for photocatalytic water-splitting hydrogen evolution, Macromol. Chem. Phys. 220 (2019) 1900304, https://doi.org/10.1002/macp.201900304.

[80] Y. Xu, N. Mao, C. Zhang, X. Wang, J. Zeng, Y. Chen, F. Wang, J.X. Jiang, Rational design of donor-π-acceptor conjugated microporous polymers for photocatalytic hydrogen production, Appl. Catal. B. 228 (2018) 1–9, https://doi.org/10.1016/j.apcatb.2018.01.073.

[81] P. Pachfule, A. Acharjya, J. Roeser, T. Langenhahn, M. Schwarze, R. Schomäcker, A. Thomas, J. Schmidt, Diacetylene functionalized covalent organic framework (COF) for photocatalytic hydrogen generation, J. Am. Chem. Soc. 140 (2018) 1423–1427, https://doi.org/10.1021/jacs.7b11255.

[82] M.Z. Rahman, M.G. Kibria, C.B. Mullins, Metal-free photocatalysts for hydrogen evolution, Chem. Soc. Rev. 49 (2020) 1887–1931, https://doi.org/10.1039/C9CS00313D.

[83] R.S. Sprick, B. Bonillo, R. Clowes, P. Guiglion, N.J. Brownbill, B.J. Slater, F. Blanc, M.A. Zwijnenburg, D.J. Adams, A.I. Cooper, Visible-light-driven hydrogen evolution using planarized conjugated polymer photocatalysts, Angew. Chem. Int. Ed. 55 (2016) 1792–1796, https://doi.org/10.1002/anie.201510542.

[84] J. Kosco, I. McCulloch, Residual Pd enables photocatalytic H_2 evolution from conjugated polymers, ACS Energy Lett. 3 (2018) 2846–2850, https://doi.org/10.1021/acsenergylett.8b01853.

[85] L. Li, Z. Cai, Q. Wu, W.Y. Lo, N. Zhang, L.X. Chen, L. Yu, Rational design of porous conjugated polymers and roles of residual palladium for photocatalytic hydrogen production, J. Am. Chem. Soc. 138 (2016) 7681–7686, https://doi.org/10.1021/jacs.6b03472.

[86] D.J. Woods, R.S. Sprick, C.L. Smith, A.J. Cowan, A.I. Cooper, A solution-processable polymer photocatalyst for hydrogen evolution from water, Adv. Energy Mater. 7 (2017) 1700479, https://doi.org/10.1002/aenm.201700479.

[87] M. Rahman, H. Tian, T. Edvinsson, Revisiting the limiting factors for overall water-splitting on organic photocatalysts, Angew. Chem., Int. Ed. 59 (2020) 16278–16293, https://doi.org/10.1002/anie.202002561.

[88] M. Qureshi, K. Takanabe, Insights on measuring and reporting heterogeneous photocatalysis: efficiency definitions and setup examples, Chem. Mater. 29 (2017) 158–167, https://doi.org/10.1021/acs.chemmater.6b02907.

[89] M.J. Frisch, G.W. Trucks, H.B. Schlegel, G.E. Scuseria, M.A. Robb, J.R. Cheeseman, G. Scalmani, V. Barone, G.A. Petersson, H. Nakatsuji, X. Li, M. Caricato, A.V. Marenich, J. Bloino, B.G. Janesko, R. Gomperts, B. Mennucci, H.P. Hratchian, J.V. Ortiz, A.F. Izmaylov, J.L. Sonnenberg, D. Williams-Young, F. Ding, F. Lipparini, F. Egidi, J. Goings, B. Peng, A. Petrone, T. Henderson, D. Ranasinghe, V.G. Zakrzewski, J. Gao, N. Rega, G. Zheng, W. Liang, M. Hada, M. Ehara, K. Toyota, R. Fukuda, J. Hasegawa, M. Ishida, T. Nakajima, Y. Honda, O. Kitao, H. Nakai, T. Vreven, K. Throssell, J.A. Montgomery, J.J.E. Peralta, F. Ogliaro, M.J. Bearpark, J.J. Heyd, E.N. Brothers, K.N. Kudin, V.N. Staroverov, T. A. Keith, R. Kobayashi, J. Normand, K. Raghavachari, A.P. Rendell, J.C. Burant, S. S. Iyengar, J. Tomasi, M. Cossi, J.M. Millam, M. Klene, C. Adamo, R. Cammi, J.W. Ochterski, R.L. Martin, K. Morokuma, O. Farkas, J.B. Foresman, D.J. Fox, Gaussian 16, Revision B.01. 2016, Gaussian, Inc., Wallingford CT.

[90] M. Kasha, Characterization of electronic transitions in complex molecules, Discuss Faraday Soc. 9 (1950) 14–19, https://doi.org/10.1039/df9500900014.

[91] N. Banerji, Sub-picosecond delocalization in the excited state of conjugated homopolymers and donor–acceptor copolymers, J. Mater. Chem. C. 1 (2013) 3052–3066, https://doi.org/10.1039/c3tc00005b.

[92] A.J. Sneyd, T. Fukui, D. Paleček, S. Prodhan, I. Wagner, Y. Zhang, J. Sung, S. M. Collins, T.J.A. Slater, Z. Andaji-Garmaroudi, L.R. MacFarlane, J.D. Garcia-Hernandez, L. Wang, G.R. Whittell, J.M. Hodgkiss, K. Chen, D. Beljonne, I. Manners, R.H. Friend, A. Rao, Efficient energy transport in an organic semiconductor mediated by transient exciton delocalization, Sci. Adv. 7 (32) (2021) eabh4232, https://doi.org/10.1126/sciadv.abh4232.

[93] K.H. Lin, A. Prlj, L. Yao, N. Drigo, H.H. Cho, M.K. Nazeeruddin, K. Sivula, C. Corminboeuf, Multiarm and substituent effects on charge transport of organic hole transport materials, Chem. Mater. 17 (2019) 6605–6614, https://doi.org/10.1021/acs.chemmater.9b00438.
[94] K.H. Lin, A. Prlj, C. Corminboeuf, How does alkyl chain length modify the properties of triphenylamine-based hole transport materials? J. Mater. Chem. C. 6 (2018) 960–965, https://doi.org/10.1039/c7tc05318e.
[95] A. Mondal, L. Paterson, J. Cho, K.-H. Lin, B. van der Zee, G.-J. Wetzelaer, A. Stankevych, A. Vakhnin, J.-J. Kim, A. Kadashchuk, P.W.M. Blom, F. May, D. Andrienko, Molecular library of OLED host materials—Evaluating the multiscale simulation workflow, Chem. Phys. Rev. 2 (3) (2021), 031304, https://doi.org/10.1063/5.0049513.
[96] H. Tetsuka, R. Asahi, A. Nagoya, K. Okamoto, I. Tajima, R. Ohta, A. Okamoto, Optically tunable amino-functionalized graphene quantum dots, Adv. Mater. 24 (39) (2012) 5333–5338, https://doi.org/10.1002/adma.201201930.
[97] E.C. Lim, S.K. Chakrabarti, Role of l→ a π transitions in Spin—Orbit coupling of aromatic amines: phosphorescence of aniline and its N-Alkyl derivatives, J. Chem Phys. 47 (1967) 4726–4730, https://doi.org/10.1063/1.1701691.
[98] E.C. Lim, S.K. Chakrabarti, Polarization of phosphorescence and symmetry of the lowest triplet state in phenoxide ion, J. Chem. Phys. 47 (1967) 4721–4725, https://doi.org/10.1063/1.1701690.
[99] J.E. Adams, W.W. Mantulin, J.R. Huber, Effect of molecular geometry on spin-orbit coupling of aromatic amines in solution. Diphenylamine, iminobibenzyl, acridan, and carbazole, J. Am. Chem. Soc. 95 (1973) 5477–5481, https://doi.org/10.1021/ja00798a008.
[100] L. Chen, C. Teng, C. Lin, H. Chang, S. Chen, H. Teng, Architecting nitrogen functionalities on graphene oxide photocatalysts for boosting hydrogen production in water decomposition process, Adv. Energy Mater. 6 (2016) 1600719, https://doi.org/10.1002/aenm.201600719.
[101] M.L. Mueller, X. Yan, J.A. McGuire, L. Li, Triplet states and electronic relaxation in photoexcited graphene quantum dots, Nano Lett. 10 (2010) 2679–2682, https://doi.org/10.1021/nl101060h.
[102] Y. Chen, J. Jayakumar, C.M. Hsieh, T.L. Wu, C.C. Liao, J. Pandidurai, C.L. Ko, W. Y. Hung, C.H. Cheng, Triarylamine-pyridine-carbonitriles for organic light-emitting devices with EQE nearly 40%, Adv. Mater. 33 (2021) 2008032, https://doi.org/10.1002/adma.202008032.